ABSTRACT

Investigation of a Trapezoidal Microchannel for Hydrodynamic Detachment of Cells or Biomolecules

Jessanne Y. Lichtenberg, M.S.B.M.E.

Mentor: Seunghyun Kim, Ph.D.

Fluid-based non-specific adsorption (NSA) methods and cell adhesion studies both use hydrodynamic forces to detach biomolecules or cells. To address the limitations in current microfluidic detachment assays and NSA removal methods, a trapezoidal microchannel was investigated as a hydrodynamic method of cell or biomolecule detachment. This design utilizes the characteristic pressure-driven flow of microfluidics to detach cells or biomolecules at the narrow region of interest while enabling flexibility in the rest of the channel with larger height and low shear stress. A fluid dynamics analysis was performed analytically and using computational fluid dynamics simulations to compare the wall shear stress and pressure drop of straight microchannels with the proposed design. The results demonstrated the trapezoidal microchannel can produce a high wall shear stress similar to a straight microchannel with the same height at the region of interest (50 μm), while conserving pressure loss, and holding a larger fluid volume.

Investigation of Trapezoidal Microchannel for Hydrodynamic Detachment of Cells or Biomolecules

by

Jessanne Y. Lichtenberg, B.S.

A Thesis

Approved by the Department of Electrical and Computer Engineering

_____

Kwang E. Lee, Ph.D., Chairperson

Submitted to the Graduate Faculty of
Baylor University in Partial Fulfillment of the
Requirements for the Degree
of

Master of Science in Biomedical Engineering

Approved by the Thesis Committee

_____

Seunghyun Kim, Ph.D., Chairperson

_____

Linda J. Olafsen, Ph.D.

_____

Yue Ling, Ph.D.

Accepted by the Graduate School

August 2019

_____

J. Larry Lyon, Ph.D., Dean

Page bearing signatures is kept on file in the Graduate School.

TABLE OF CONTENTS

LIST OF FIGURES

LIST OF TABLES

ACKNOWLEDGMENTS

Thank you to my advisor, Dr. Seung Kim, for the opportunity to develop this study and for his guidance. He has been an incredible advisor, professor, and mentor throughout my college career. Thank you also my committee members for their excellent advice and guidance: Dr. Ling in his help with the CFD simulations and Dr. Olafsen in her thorough evaluation of this thesis. Thank you to my fellow members in the Bio and Micro Devices Lab for their willingness to help me and their camaraderie.

Thank you to my friends near and far for your prayers and encouragement. Thank you to my family, especially my parents, for always believing in me and supporting me in every endeavor I have pursued. Thank you to my fiancé, Logan, for your patience during this time and support for my education. Thank you to God, for all His blessings and for allowing me this opportunity.

DEDICATION

To my Mom and Dad

CHAPTER ONE

Background

Cell Adhesion

Cell adhesion is the ability of a cell to affix to another cell or an extracellular matrix (ECM). An ECM is a three-dimensional network of extracellular macromolecules, such as collagen, enzymes, and glycoproteins, that provides structural and biochemical support of surrounding cells. Cell adhesion has been broadly investigated for many cellular biology and biomedical applications [1]. Numerous methods have been developed to measure cell adhesion to better understand cell signaling pathways, tissue engineering, biomaterial studies for implantable sensors, cancer metastasis study, and the adhesion properties of normal and cancerous cells. Requirements for cell adhesion are different for various applications, and are dependent on specific applications [1].

Cells have adhesion sites, formed by transmembrane proteins called integrins, that anchor the cells to an ECM or other cells. The focal adhesion (FA) complex is how the integrins and adhesion molecules attach to the tensile members of the cytoskeleton [1]. The formation of FA's is important in cell signaling to direct migration, proliferation, and differentiation. Based on the cell adhesion model, the more a cell sticks, the more chemical bonds are on the surface.

Passive *in vitro* cell adhesion occurs in a static medium culture, such as a petri dish. There are three stages in static *in vitro* cell adhesion: attachment of the cell body to the substrate, flattening and spreading of the cell body, and the organization of the actin

skeleton with the formation of FA [1]. In dynamic *in vitro* cell adhesion, such as the adhesion of cells to ECM under blood flow, shear flow is a vital factor to initiate cell adhesion. The adhesive bond is a combination of non-covalent interactions, including hydrogen bonds, electrostatic interactions, van der Waals forces, and dipole-dipole interactions. Cell adhesion can be classified into attachment or detachment events, which can be further categorized as single-cell or population approaches. There are numerous techniques that have been developed for these approaches, as described in the recent review by Khalili and Ahmad. Single-cell attachment events are studied via micro patterning, polyacrylamide gel based traction force microscopy (PA-TFM), and 3D hydrogels. Cell population attachment events are studied through wash assays, resonance frequency, and microfluidics (Fig. 1.1.b).

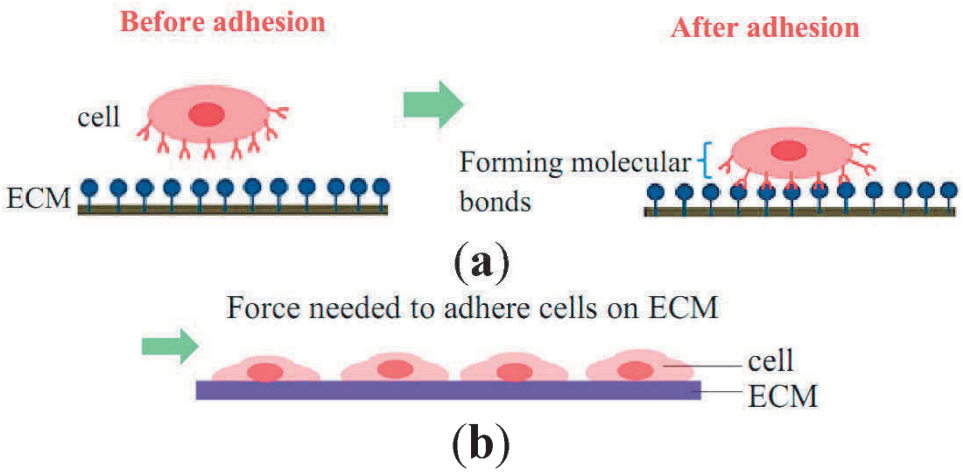

Figure 1.3. Schematic diagram of cell adhesion attachment events for (a) single cell studies via formation of molecular bonds; and (b) cell population studies via dynamic adhesion (e.g. microfluidic technique). Adapted from Ref. [1]

Microfluidics is the field of fluid handling technology involving very small volumes of liquids in the range of 10^{-6} to 10^{-18} L [2]. Microfluidics have numerous applications including biomedicine, cell analysis, drug screening, cell biology, and

biosensing [2]. In recent years, momentous work has been done to reduce the size of conventional biosensors using microfluidics for lab-on-a-chip practices [3]. Numerous benefits exist for using microfluidics such as the low consumption of costly reagents, minimal handling of hazardous materials, short reaction time, multiple sample detection, increased portability and design versatility [3].

Cell Detachment

Cell adhesion detachment studies involve applying a load to the adhered cells on the ECM to free the cells from their bonding (Fig. 1.2). Measuring the adhesion strengths of cells is a popular interest when studying biomaterial compatibility, cancer cells, drug treatments, and the discovery of biomarkers for early disease detection. The applied force that produces the cell detachment is quantified as the cell's adhesion strength. The force or stress value when 50% of the cells detach is determined as the population adhesion strength. Single cell approaches to study detachment events include cytodetachment, micropipette aspiration technique, microfluidics, single cell force spectroscopy, atomic force microscopy (AFM) probe force measurement, and biomembrane force probe [1].

There are four main methods of studying cell population detachment events: centrifugation, spinning disk, flow chamber (radial and parallel), and microfluidics [1]. Of these methods, centrifugation and spinning disk do not allow for real-time analysis, or the exploration of cell behaviors under diverse experimental conditions. A key limitation of conventional parallel plate flow chambers is their inability to generate shear stresses large enough to detach well-spread cells while maintaining laminar flow [4]. Additional limitations include lack of ability to generate multiple shear stresses simultaneously, variability in device thickness, and complication in assembly processes [5]. Furthermore,

radial and parallel flow chambers are generally limited to short term adhesion studies [1], [4]. Long term cell adhesion studies are important for mimicking *in vivo* conditions,. Typical parallel flow chambers are capable of producing a maximum shear stresses on order of 10 Pa under laminar conditions [4].

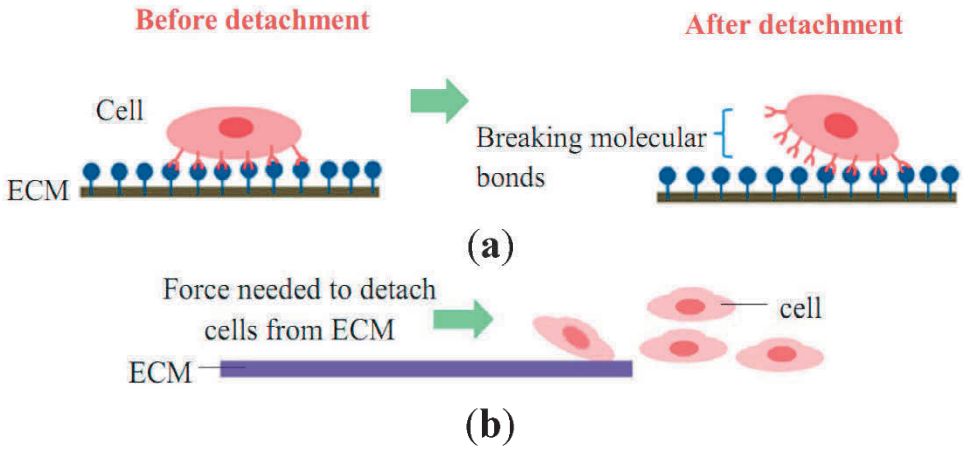

Figure 1.4. Schematic diagram of cell adhesion detachment events for (a) single cell studies via breakage of molecular bonds (e.g. optical tweezer, micropipette aspiration); and (b) cell population studies via dynamic adhesion (e.g. spinning disk, flow chamber, and microfluidic technique). Adapted from Ref. [1]

The use of hydrodynamics in cell studies is vital, because the hydrodynamic effects influence multiple cellular properties and processes [6]. Additionally, the effects can be used to control mechanical stresses, analyte transport, and local temperature within cellular microenvironments. For studies investigating cellular response to mechanical stimuli, contact-based studies, such as those using probes to induce the stimulus, are unfavorable because a fragile cell can be damaged. In contrast, microfluidic-based platforms enable the ability to deliver controlled shear and mechanical stimuli, thus providing a favorable tool for studying the mechanosensitivity of cells. Shear stress affects the morphology and fate of many cell types, including endothelial,

smooth muscle, and osteoblast. Fluid shear stress influences calcium dynamics, resulting in deviance in bone cell function and remodeling. Low shear flow affects the motility of cells and hydrodynamic forces can also affect cell differentiation and phenotyping.

Biosensors

Global health is the practice of providing adequate healthcare worldwide [7]. However, the aging population and increased diseases worldwide make this task difficult, even more so in resource-limited environments. In the past couple of decades, the trend of diagnostic devices for the early identification of disease and routine health checks have become a popular research topic to aid in global health. These point-of-care (POC) devices are designed for use outside of the hospital setting, at the bedside, or in limited resource environments. The World Health Organization defined characteristics for a POC diagnostics using the acronym ASSURED: Affordable, Sensitive (avoid false negative results), Specific (avoid false positive results), User-friendly, Rapid and Robust, Equipment-free, and Delivered (accessible to end users) [8].

Biosensors are an interdisciplinary field that is currently one of the most active areas of research in analytical chemistry [9]. Biosensors are used in a variety of applications from food processing, environmental monitoring, medicine, military technology, and iotechnology [5]. Here, the focus is biosensors for medical diagnostics. Common biosensor examples are a blood-glucose monitor used by a diabetic patient and a pregnancy test that measures the amount of the hormone hcG (human chorionic gonadotropin) in a urine sample. A biosensor can be defined as a device that measures an certain amount of a biological sample and interprets the data into a signal readable by the user [2]. The main parts of a biosensor are the analyte, the bioreceptor or recognition

element, transducer, and display element (Figure 1.3). The analyte is contained in the biological sample being detected and could be DNA, proteins, cells, or exosomes. The bioreceptor is the molecule that binds to the analyte. The interaction of the bioreceptor to the analyte creates a signal measured by the transducer. The transducer converts the signal into a readout the user can easily understand.

The interaction between the bioreceptor and analyte can be categorized into affinity or catalytic [2]. Affinity biosensors are based on the binding affinity between the analyte and bioreceptor (e.g. antibody-antigen). In catalytic biosensors a chemical reaction produces a product which can be correlated with the concentration of target analyte. An example of a catalytic sensor is a glucose biosensor which uses the enzyme glucose oxidase that catalyzes the oxidation of glucose to hydrogen peroxide.

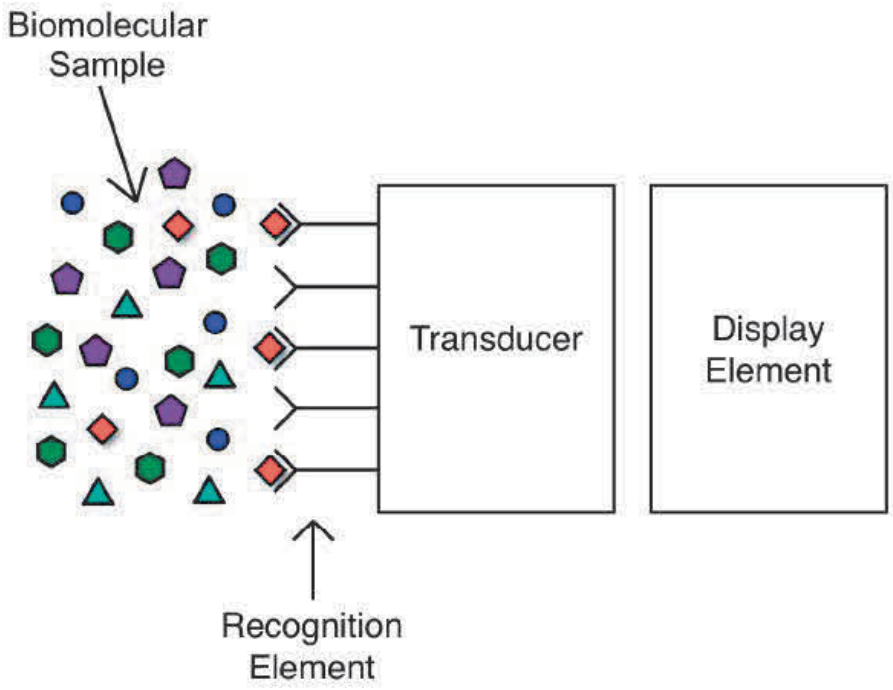

Figure 1.5. Diagram of typical biosensor architecture [10].

Biosensors can be classified by the bioreceptor or by transducer [2]. Classifications by biorecognition element include: nucleic acid, aptamer, antigen/antibody (immunosensor), enzyme, or cell. Classification by transduction mechanism includes: optical, electrochemical, and piezoelectric or mechanical [2]. Some examples of optical transduction methods include colorimetric and fluorimetric. Electrochemical sensors can be further categorized into amperometric, voltammetric, resistive, or impedimetric.

The performance of a biosensor is usually experimentally evaluated based on its sensitivity, limit of detection, linear and dynamic ranges, reproducibility of the response, selectivity and response to interferences [9]. Sensitivity is the value of the electrode response per substrate concentration [11]. Linearity of the sensor should be high for the detection of high substrate concentration. Selectivity means chemicals interference must be minimized for obtaining the correct result. Additional parameters include the sensor's response time (defined as the time after adding the analyte for the sensor response to reach 95% of its final value), operational and storage stability, ease of use, and portability [9], [11]. All of these characteristics are highly important parts of biosensor. Therefore, to design a biosensor, analyte, sample handling, bioreceptor and transducer must be wisely chosen [11]. A model biosensor contains functional areas coinciding with the sensing area and inactive areas everywhere else to promote minimum sample consumption [12].

Creating sensitive, selective, and stable biosensors for the timely identification of disease biomarkers is greatly important [13]. In recent years, copious research has been focused on the development of new methods for early disease detection [13]. Numerous in-depth reviews on biosensors exist for readers of interest [2], [9], [14], [15]. The goal

for a biosensor is to achieve the maximum sensitivity, specificity and selectivity for a particular application [12]. Most chemical and biological sensors used today are based on classical standard enzymatic or fluorescence-labeled methods such as enzyme-linked immunosorbent assay (ELISA) or fluorescent microscopy, where target molecules are modified by labeling [3]. However, the labeling procedure is time-consuming, labor-intensive, and often difficult to accurately quantify results because of different labeling efficiencies for targeted proteins. A number of label-free sensors have reportedly overcome those limitations, including surface plasmon resonance (SPR) sensors. While SPR is a promising tool for ultrasensitive, real-time and high-throughput detection, label-free biosensors, including SPR biosensors, often suffer from severe non-specific adsorption (NSA) of proteins. Protein NSA causes false positive errors in detection through overestimation of the affinity value, which will be discussed more later.

Decreasing the sensor dimensions also enhances signal-to-noise ratio by increasing the signal density and reducing background signals [16]. Literature on the design and applications of microfluidic biosensors is vast [15], [17]–[20]. Microfluidic biosensors often have immobilized bioreceptors, such as antibodies [21], enzymes [22], DNA [23], or linker molecules such as SAMs (self-assembled monolayers) to improve surface immobilization. However, the linker molecules are prone to NSA, resulting in decreasing sensitivity and false responses [3].

Challenges

While biosensors are a popular research topic, there are still challenges to be overcome in this field. Mainly, these obstacles include commercialization [24], mass-transport limited sensing [25], and NSA [26]. Despite the numerous improvements and

ongoing research, the commercialization of biosensors for infectious diseases is still premature [24]. The integration of the detection, sample preparation, and transducer into a self-contained, automated system is the most critical challenge for POC biosensors [24].

Under fast flow conditions (when convective flux is greater than diffusive flux), there is an increased flux to the sensor surface [25]. However, many molecules will flow past the sensor without having a chance to interact with the surface and thus lowering the capture efficiency. This is the issue of mass-transport limited sensing. The transport of molecules to the sensing surface, a key aspect of sensor design, is rarely discussed in depth. For the detection of low-abundance analytes, the rate of molecular transport from the bulk solution to the sensor surface is especially important. When an analyte solution comes into contact with a sensor surface, molecules close to the surface will bind to the receptors. This will cause the region adjacent to the sensor surface to become depleted of target molecules and form a depletion layer. This creates a concentration gradient which will trigger a flux of molecules toward the sensor surface; this is the main transport mechanism for target molecules to reach the surface.

Non-Specific Adsorption

The other main challenge to be overcome in biosensor development is that both the sensor element and the neighboring surfaces have to be unreactive to NSA. Also known as non-specific binding or biofouling, NSA is a persistent challenge in biosensing [3], [15], [27]–[29]. While NSA is also an issue in other biological fields including implantable biomedical devices [1], [30], [31], and marine equipment [32], [33], this report will focus on NSA for biosensing applications. Most biomolecular surfaces,

whether comprised of antibodies, enzymes or proteins, experience the common issue of hindrance from non-specific species [27]. For biosensors, the molecules typically adsorb to the sensing surface from a liquid medium. It is imperative to limit the attachment of target molecules to the sensitive areas of the sensor by subsequent specific functionalization. Especially for small-scale sensors, it is crucial to accomplish controlled patterning of functional molecules. This is because the size of the molecules used for passivation and capture, as well as the analytes of interest, have similar dimensions to the sensor element or at least comparable to the size of the sensitive area [12].

Surface-based sensing is a common method of biosensing, exemplified by immunosensors (*e.g.* ELISA and SPR), microfluidic biosensors, and electrochemical biosensors. However, biomolecular areas of surface-based sensors often come into contact with complex mixtures of proteins and other molecules during their use [34]. Most surfaces are particularly prone to non-specific and irreversible adsorption of proteins, known as NSA [3], [34]–[36]. NSA happens when a molecule adsorbs to a sensor's surface, resulting in high background signals that are indiscernible from the specific binding [35]. This phenomenon occurs because of physisorption and can decrease the sensor’s performance [13], [35].

Adsorption is the adhesion of atoms, ions or molecules from a gas, liquid or dissolved solid to a surface [37]. There are two types of adsorption: physical and chemical. Physical adsorption, or physisorption, results from intermolecular forces including hydrophobic forces, ionic interactions, van der Waals forces, and hydrogen bonding. Chemical adsorption, or chemisorption, results from chemical interactions such

as covalent binding. In NSA (Fig. 1.4), molecules are adsorbed to a surface through the weaker adsorption, physisorption [35].

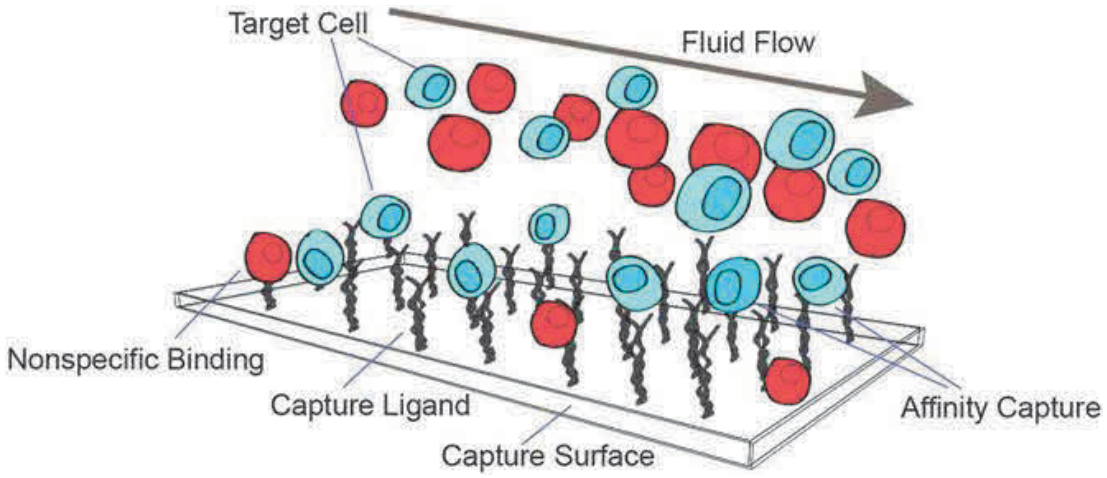

Figure 1.4: Target molecules (blue) in a sample containing background cells (red) flow through a microchannel. The surface is covered with bioreceptors. Affinity capture is when the receptors on the target cell are recognized by the capture ligand. Non-specific binding occurs when a background cell binds to the ligand or the channel surface without forming ligand-receptor bonds. Adapted with permission from Ref [38]. Copyright 2018 John Wiley and Sons.

Immunosensors, a common type of biosensor, use antibodies or antigens as the bioreceptor. For antibodies, there are two types of non-specific adsorption: immunological and methodological. Immunological has more to do with the affinity between the antibody and antigens, and cannot be improved without using different proteins. Methodological non-specificity can occur due to a variety of reasons, but is usually a combination of protein-protein interactions, surface protein denaturation or mis-orientation, substrate stickiness, non-specific electrostatic binding to charged surface, and adsorption of molecules in free spaces [27]. This phenomenon can result in four different types of NSA: (1) molecules adsorbed on vacant spaces (2) molecules adsorbed on non-immunological sites (3) molecules adsorbed on immunological sites, allowing access to

antigens and (4) molecules adsorbed on immunological sites. Non-specific adsorption leads to elevated background signals that cannot be discriminated from specific binding [35]. These false-positive signals affect the dynamic range [27], limit of detection [9], [35], reproducibility, selectivity, and sensitivity [35]. The reduction of NSA is crucial in the development of biosensors, especially for point-of-care clinical diagnostics.

Numerous methods exist to reduce non-specific interactions on sensing surfaces. Passive methods aim to reduce NSA by blocking or coating the surface, while active methods generate surface shear forces to overpower the adhesive forces of the non-specifically adsorbed molecules [35]. Surface shear forces can be generated by a transducer or hydrodynamically. Transducer-based active methods are typically categorized as electromechanical or acoustic devices. Another less commonly used technique is hydrodynamic removal, which relies solely on the fluid flow to generate the shear forces. Chapter Two will further this discussion of NSA reduction methods, focusing mainly on the less discussed active methods.

CHAPTER TWO

Review of Non-Specific Adsorption Removal Methods in Biosensing

Non-specific adsorption (NSA) is a challenge in developing a highly sensitive and specific biosensor. Proteins are the most commonly discussed and used biologically-derived recognition element [12]. Therefore, many NSA reduction methods are focused on proteins. Limiting NSA has been investigated for decades [39]. Recent reviews focus on NSA reduction for certain sensor types such as the suppression of protein NSA in the development of electrochemical immunosensors [28], antifouling materials for SPR sensors [40], nanoscale sensors [12], and whispering gallery mode optical biosensors [41]. With the increased trend in micro/nano-scale biosensors, a shift from passive methods to active removal methods is noticed in literature, which is discussed in depth in this chapter.

It is important to note that for some sensors, NSA can be distinguished from the analyte signal. This is the case for biodetection with attenuated total internal reflection Fourier transform infrared (ATR-FTIR) or ellipsometry. ATR-FTIR spectroscopy have been used for biotin detection, where the specific binding was able to be differentiated from the non-specific protein binding [42]. Ellipsometry, which measures the change of polarization upon reflection or transmission, has been used to study in vitro polyclonal antibody adsorption [43]. This technique can be used to identify the specifically adsorbed proteins from a complex solution. However, this method is not successful for monoclonal antibodies, and requires an optically reflective, flat surface. Infrared (IR)

ellipsometry has been demonstrated as a label-free imaging method to map different materials on a biochip [44]. Compared to conventional chemiluminescence imaging, this method was found to be able to map larger sample areas with greater resolution (300 μm x 300 μm), attained by using radiation from an IR synchrotron beamline. While imaging techniques are useful for discriminating between specific and non-specific adsorption, their implantation is not applicable to all sensors. A majority of surface-based sensors suffer from the effects of NSA, particularly microfluidic biosensors.

Non-specific adsorption can be reduced by a number of approaches with varying complexity [34]. NSA reduction methods can be generally divided into two categories: passive methods and active methods (Figure 2.1). The passive methods aim to prevent undesired adsorption by coating the surface, and can broadly be sub-categorized as physical and chemical. These methods have existed for several decades and are vast in the literature. In contrast, active methods dynamically remove adsorption post-functionalization and are a more recent technique. Active removal methods can be further categorized as transducer-based or fluid-based. The transducers used are typically electromechanical or acoustic. Fluid-based methods utilize the pressure-driven flow of microfluidics to shear away molecules. This review will briefly describe the passive methods, which have been thoroughly described in the literature already [3], [27], [28], [32], [45], while focusing on the active methods which have yet to be thoroughly investigated.

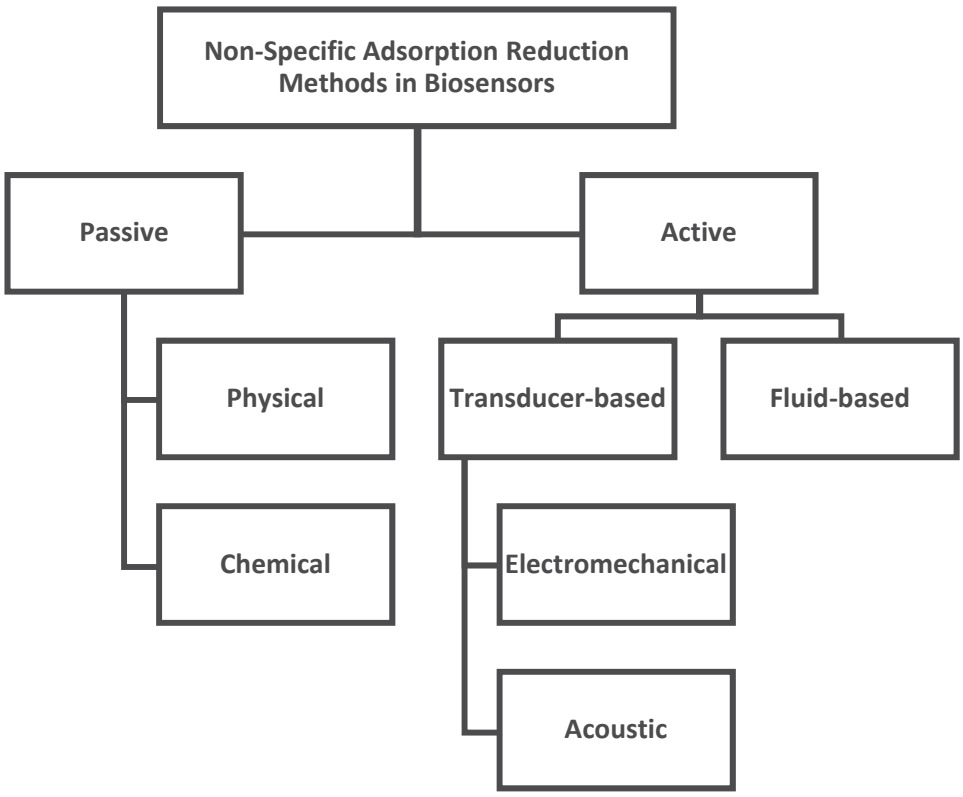

Figure 2.1. Chart outlining the main mechanisms of NSA reduction (passive and active) and sub-categories of each.

Passive Methods

Blocking methods can be categorized into two broad categories: physical (i.e. protein blockers) and chemical (i.e. linker molecules). A recent review has provided an in-depth review of physical and chemical surface modification methods [12]. Therefore, here we will only briefly summarize the main mechanisms in this review and note key examples. Passive methods aim to create a thin hydrophilic and non-charged boundary layer to thwart protein adsorption [35]. The goal of anti-fouling coatings is to minimize the intermolecular forces and interactions between the adsorbing molecules and the host substrate so the molecules can be easily detached and released under low shear stresses,

like washing [46]. Materials for non-fouling coatings are usually neutral or weakly negative and well hydrated [45].

Physical

Physical surface modification does not typically change the chemical composition of the surface. The most popular and easiest method to prevent NSA is to use blocker proteins that adsorb to surfaces. For example, serum albumins [47], [48], casein [48], [49], and other milk proteins [48] are commonly used as blocking agents for enzyme-linked immunosorbent assay (ELISA), Western blotting, and other enzyme based assays [48], [50], [51]. The underlying assumption of these methods is the idea that a controlled patterning of the surface-active protein will inhibit the immobilization of other molecules to the substrate [34]. Commonly used bovine serum albumin (BSA), a protein derived from cows, is easily accessible and inexpensive [47]. However, the usage of BSA often leads to a non-uniform layer on the surface, and studies have reported proteins can still adsorb to a BSA layer [34]. Additionally, while protein blockers can be applied to a variety of surface materials, they can have high lot-to-lot variability, cross-reactivity [52] and alter the original surface properties [53].

For catalytic biosensors, a permselective membrane, which has preferential permeation of certain ionic species through ion-exchange membranes, can be used to reduce NSA [19], [54], [55]. In an amperometric glucose sensor, the ion permselectivity avoids interfaces of the detection of hydrogen peroxide by ascorbate, urate and acetaminophen [19], [56]. Additionally, the use of a permselective membrane can reduce the influence of buffer concentration on the sensor signal [57]. Another method of dealing with protein NSA utilizes the Vroman effect [19], [58], [59]. This is when a weak

affinity protein bound to the surface is displaced by a strong affinity protein [19]. The reverse operation does not occur. This phenomenon is due to the fact that protein adsorption capability is largely dependent on the molecular weight [60]. Therefore, in general, a high molecular weight protein adsorbs more strongly than a low molecular weight protein. The displacement of these proteins can be measured by SPR [61].

Chemical

Chemical methods of anti-fouling include using a poly(ethylene glycol) (PEG)/oligo(ethylene glycol) (OEG) based coating [35], [46], [62], [63], functionalized self-assembled monolayers (SAMS) [3], [35], [64]–[67], or zwitterionic polymers [13], [35], [45], [68]–[70]. PEG is a non-ionic, water soluble polymer commonly used to form protein-resistant layers [63]. PEG and OEG have been widely used antifouling materials due to their surface hydration [13], and weakly basic ether linkages [46]. However, they are vulnerable under oxidative conditions, which limits their efficacy for long-term applications [13], [63]. Additionally, the auto-oxidation of the terminal hydroxyl group in PEG into aldehydes can deteriorate the specific proteins used for sensing [71]. Some types of PEG are only useful for negatively-charged surfaces, and are most successful with metal oxide surfaces [34]. These compounds are better suited for single proteins, but most often fail in complex mixtures of proteins (e.g. blood plasma [72], [73]), or under *in vivo* conditions [74]. Furthermore, the density and chain length of PEG need to be optimized for minimizing non-specific interactions [62]. The ability of PEG to prevent NSA depends on other parameters, such as temperature [73], and can be unstable [75]. Researchers have used nanostructured surface coatings to reduce protein adsorption as an alternative to polymer modification [76].

Self-assembled monolayers (SAMs) offer an oligoethylene glycol functional group at the solid-water interface [34]. Alkanethiol SAMs are one of the most popularly used bioreceptor linker molecules, due to the two major advantages: plentiful functional groups to immobilize bioreceptors and a dense monolayer that allows little NSA [3]. Sensing surfaces with alkanethiol SAMs suffer from NSA due to three main reasons: polycrystalline gold grain structure, imperfectly formed monolayers, and non-immobilized bioreceptors [3]. Additionally, factors such as surface roughness, annealing, and the use of short or long chain SAMs can affect the results [3]. Furthermore, oligoethylene glycol-terminated SAMs are only compatible with gold and silver surfaces [34], which limits their use considering the variety of substrates used today in biosensing [34], [71].

Zwitterion polymers or polyzwitterions are polymers made up of zwitterions, molecules which have both a positive and negative charge [70]. Zwitterion polymers have the same number of anionic and cationic groups, so the overall charge is zero under normal conditions [70]. These ionic groups repel unwanted adhesion with a strong hydration layer through ionic solvation [13], [46] and are functional over a large pH window [70]. Zwitterionic polymer brushes may be grafted to or grafted from surface [70]. However, most zwitterionic reagents that can be presented onto substrate surfaces for NSA reduction are usually restricted to betaine and phosphorylcholine related chemicals, whose synthetic processes are slow and difficult [13]. A promising subclass of zwitterionic polymers is polyampholyte polymers, composed of mixtures of charged monomer subunits, whose mechanical properties of the polymers can be tailored. Surface

grafted polyampholyte polymer brushes have been demonstrated as an anti-fouling coating for sensing applications in complex media [77].

Challenges with chemical methods include laborious functionalization processes, long-term chemical stability, raising the sensor background signal [35], and prospect to damage active surface [35], [71]. Additionally, some chemical methods have limitations in transducer interfaces as previously described [34], [35]. The prevention of NSA with passivation methods often involves the use of harsh chemicals that are normally not appropriate for many biological uses [34].

Manipulating surface chemistry is only part of controlling protein adsorption. The surface topography is key in determining the structure of bound proteins [78] and can be used to control specific protein adsorption [79]. Alternative methods to control NSA is through the patterning or imprinting the surface with a unique surface topography or synthetic polymer. Shi *et al.* reported a method of imprinting surfaces with nanocavities to specifically recognize template proteins [79]. The authors suggest non-template proteins will be less likely to attach to the imprinted sites because they lack the ability to interlock in the cavities and form a strong bond. The imprinted surface topography was evaluated using tapping-mode atomic force microscopy (AFM). They evaluated three imprinted blood proteins (BSA, IgG, and fibrinogen) compared to a flat control surface, and found a higher number of proteins were adsorbed on the imprints. After using a detergent to clean the surface, the researchers found the protein imprint retained more of the proteins than the control surface, implying a greater affinity at the imprinted cavities. Specific binding sites can be limited to the nanocavities, while elsewhere is blocked with BSA passivation. Roach *et al.* investigated the effect of surface topography on the

binding of proteins [78]. They found differences in how certain protein geometries were affected by surface structure. For example, a globular protein like albumin, is more compatible with a surface with high curvature. However, a rod-like protein such as fibrinogen, is distorted by a curved surface, which promotes structure loss. These effects are important when considering how to optimize specific adsorption and prevent NSA [78].

A synthetic recognition system can also be implemented as an alternative to the typical biological receptor used in sensing [80], such as molecularly imprinted polymers (MIPs). This synthetic recognition system is inexpensive, easy to implement, and allows target species to rebind to the imprinted sites. However, challenges exist the uncontrolled random polymerization produces uneven imprinted sites. Additionally, the use of MIPs is limited to chemical detection or bioassays due to the inability to generate signal output at the surface of the transducer. Molecularly imprinted nanomaterials, such as nanowires, nanotubes, nanofibers have been investigated for chemosensors as a solution to the challenges faced by traditionally imprinted materials. While improvement in achieving sensitive detection has been achieved with these methods, there are still limitations to this method including the need to enhance the specific binding, reduce NSA, and allow for multiplexing and easy integration [80]. Due to these limitations, active methods have emerged as an alternative to combat NSA.

Active Methods

Methods of active NSA removal have emerged in the past decade as a promising approach to reduce NSA in biosensors. These methods produce surface shear forces, which are stronger than the adhesive force of the weakly bound NSA molecules.

Meanwhile, the specific proteins are not removed because the affinity of specific proteins toward a ligand is several orders of magnitude larger than that of non-specific proteins [26], [81]. Transducer-based approaches can be used for numerous types of proteins, making them time-saving, easy operating, and efficient methods for removing NSA [35]. Transducer devices to remove NSA can be categorized as electromechanical or acoustic (Fig. 2.1) [35]. A summary of active NSA removal methods is provided in Table 2.1.

Transducer-based

The shearing forces in electromechanical methods are generated from the electrical or mechanical transducers. Some examples of electromechanical methods include ac-EHD (alternating current electrohydrodynamics) induced nanoshearing [36], [82]–[85], hypersonic resonance [35], and resonant cantilever vibration [53].

A sensor has been developed that uses ac-EHD induced surface shear forces, or nanoshearing, to improve the analyte capture of the sensor and remove weakly (non-specifically) bound molecules from the electrode surface [36]. The working principle is that the ac-EHD induced flow generates shearing forces within nanometer distances of the electrode surface to produce lateral fluid flow (Fig. 2.2a). This not only mixes the fluid around the sensor surface to enhance capture efficiency through increased sensor-target collisions, but the ac-electric field can enable selection of specifically bound proteins over non-specifically bound proteins (Fig. 2.2b). This produced 100 fg mL^{-1} naked eye detection of multiple protein targets spiked in human serum [36]. The results were compared to that of a pressure-driven flow system with the same flow rate. The authors found the absorbance measurements were 1000 times better for the ac-EHD system than the hydrodynamic. Additionally, they noted limitations of pressure-driven

flow including the stationary boundary layer of fluid, which does not allow for surface shear force manipulation, and the external syringe pump needed that is not easily integrated into portable devices. This system is multiplexible via several individual channels for distinct functionalization of different bioreceptors. This device has been applied for sensing and biofouling of cancer cells [84] and exosomes [83] as well as being incorporated with a surface-enhanced Raman scattering (SERS)-based immunoassay [85]. A complete look at ac-EHD use in microsystems has been recently published for the interested reader [86].

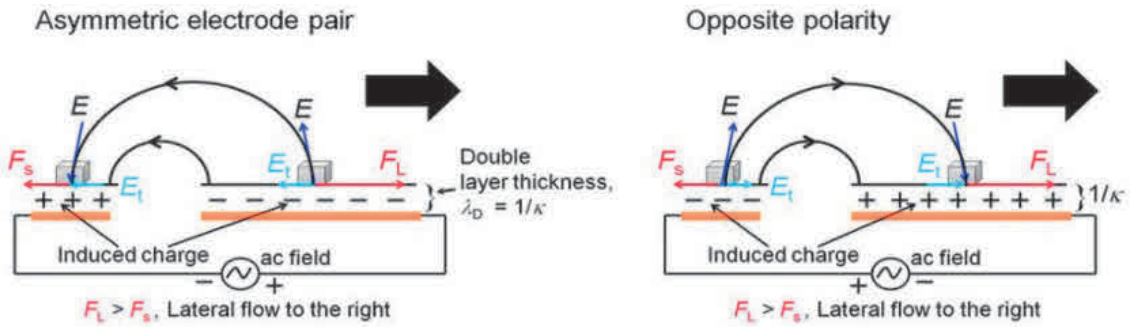

(a)

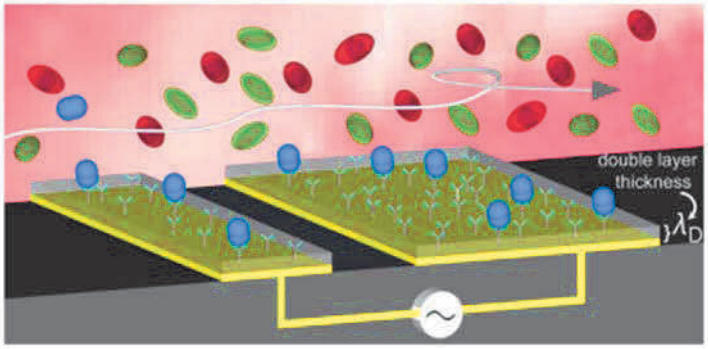

(b)

Figure 2.2. ac-EHD induced fluid flow (a) Mechanism of how the electric field induces charges in the double layer of each electrode experience. Adapted with permission from ref [65]. Copyright 2014 Springer Nature. (b) Schematic of ac-EHD induced nanoshearing. The target proteins (blue) are bound to the bioreceptors while the non-specifically bound molecules (green and red) are removed. Adapted with permission from ref [36]. Copyright 2015 Springer Nature.

Table 2.1. Summary of Active NSA Removal Methods.

Category	Type	Analyte	Ref.
Transducer-based			
Electromechanical	Hypersonic Resonance	Cy3 labeled human IgG antigen	[35]
	ac-EHD	PSA [36]; IgG [36]; HER2 [36], [82], [85]; HER2 & PSA exosomes [83]; MCF7 & T-47D cells [84]	[36], [82]–[85]
	Resonant Cantilever Vibration	BSA	[53]
Acoustic Wave	Surface	None (simulated) [71], [87] IgG antigen [88]	[58], [70], [71]
	Orthogonal Surface	None (simulated) [26]	[26], [89]
	Longitudinal	Biotinylated GNP-GSC	[90]
	Piezoelectric	Avidin	[47]
	Bulk	Proteins [91] None (simulated) [92]	[91], [92]
Fluid-based			
	Hydrodynamic	HER2	[93]

Since the shearing forces typically come from electrical or mechanical vibration of the devices, the NSA removal is limited to the proteins adsorbed on the transducer surface [35]. Pan *et al.* proposed a solution to this problem by using a microfabricated 2.5 Ghz hypersonic resonator to generate microvortexes in the fluid, which results in the attenuation of acoustic energy into the liquid (Figure 2.3) [35]. The resulting drag and lift forces along the liquid-solid interfaces were used to control the NSA removal. The experimental results supported the mathematical and simulated models. The proteins were modeled as spherical proteins with a diameter of 100 nm, which correlates to a 500 mW power to remove them. However, if the proteins are 1-10 nm, the required power is very high, ~5W. The mass-sensitive hypersonic resonator displayed a shift in the resonance frequency as each step was performed. However, frequency change cannot differentiate between specific or nonspecific binding. Therefore, fluorescent microscopy was used to verify the NSA removal with a specific immunoglobin G (IgG) and nonspecific IgG. The quantitative testing showed an 83.8% fluorescence intensity decrease for the nonspecific binding sites after hypersonic treatment and only 6.1% with specific binding sites. Additionally, the vertical orientation of the vortexes allows a contactless setup, which enables the resonator to be combined with other surface based biosensors. The detachable actuator enables reuse. The authors determined the drag force was the primary force in removing NSB.

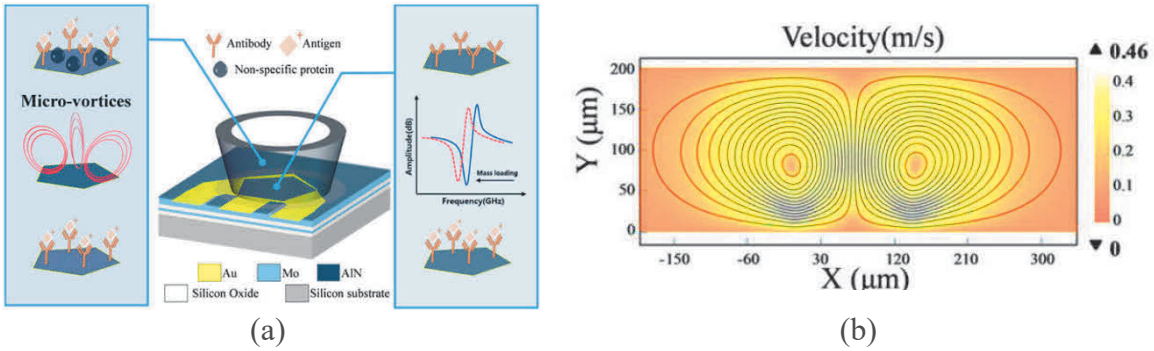

(a) (b)

Figure 2.3. Hypersonic resonator for biofouling removal and protein detection: (a) Illustration of microvortexes in liquid triggered by the hypersonic resonator; (b) Simulation of the fluid motion triggered by the hypersonic resonator. Adapted with permission from Ref [9]. Copyright 2017 the American Chemical Society.

Johnson and Mutharasan demonstrated that transverse modes in electrochemical piezoelectric-excited millimeter-sized cantilevers (ePEMCs) caused the release of adsorbed bovine and human serum albumin proteins from sensor surfaces [53]. They first determined ePEMC transverse mode vibration does cause streaming and tested different excitations voltages and particle concentrations. Then, they tested the release of BSA and human serum albumin (HSA), and repeated the experiments with thiolated single-stranded DNA strands to Au sites, which has a 4 times higher binding energy than BSA. The results were determined through electrochemical and mass change sensing techniques, and further verified with wet chemical-based spectroscopic analysis. The study found the release of the NSA proteins was caused by a combination of surface strain energy, body forces, and acoustic streaming associated with hydrodynamic effects. Furthermore, this work could be applied to removing specific binding for bioseparation and diagnostic applications. Before this work, few studies had investigated the non-specific interactions of the non-target species [94]. In recent years, the use of micro

cantilever-based sensing systems has increased due to their anticipated high sensitivity [94]–[100].

Acoustic wave sensors use acoustic energy to disturb the bonds between the sensing layer and analyte, coercing only the molecules with the higher affinity (i.e., specific proteins) to stay attached. The fluid motion induced from high-intensity sound waves is called acoustic streaming [71], [101], [102]. The produced sound fields cause tangential fluid motion along the fluid boundaries. The fluid motion applies a steady viscous stress on the boundary layer, causing liquid circulation near the boundaries. These stresses are strong enough to remove loosely bound molecules on the surface of the device. Acoustic streaming enables higher accuracy measurements and reusability of the devices [71]. Examples of acoustic transducer devices include surface acoustic wave (SAW) [71], [87], [88], orthogonal SAW [26], longitudinal acoustic wave (LAW) [90], and bulk acoustic wave [91], [92]. Detailed information on acoustic sensing has been recently published [103]–[108].

Combined electromechanical systems are under investigation too. A nanomolecule desorption mechanism was demonstrated using a combination of electric field and mechanical vibration to remove BSA and IgG from metal coated lead zirconate titanate (PZT) surfaces (Fig. 2.4) [74]. Surface acoustic waves propagating on the surface of a piezoelectric device can be used to induce acoustic streaming within the fluid [71]. Previous studies demonstrated the ability of Rayleigh wave modes to release NSA proteins from the surfaces of SAW devices [88]. The acoustic waves generated from the piezoelectric coupling successfully induced fluid motion (acoustic streaming) and physically forced weakly bound non-specific protein species from their binding sites,

improving the biosensor response [88]. The work was furthered by using fluid-solid interaction models to explore parameters for elevating induced acoustic-streaming velocities and forces to eradicate biofouling, while minimizing the effect of streaming-induced removal forces on the antibody sensing layer in immuno-SAW sensors [71]. Singh *et al.* reported multi-directional transducer-based SAW devices on a single piezoelectric platform produces the benefit of carefully using aspects which are particular to acoustic waves spreading along a given crystallographic orientation [26].

Hsu *et al*. used a piezoelectric transducer to produce varied amplitude and swept-frequency longitudinal acoustic waves remove non-specifically bound biomolecules (Fig. 2.5) [90]. They used a sample chip composed of a diced glass slide chip (GSC) modified with gold nanoparticles (GNPs) and immobilized biotin as a probe [90]. The absorbance spectra of the localized surface plasmon resonance (SPR) band were used for quantitative analysis of the removal efficiency [90]. They demonstrated that even strongly bound streptavidin molecules were able to be removed from the biotin-functionalized GNP-GSC surface [90]. The study also aimed to investigate the regeneration of specific binding sites. The device was found to be reusable at least five times for regeneration, and the NSA removal ability was tested with four different adsorbing molecules: BSA, streptavidin, anti-biotin, and anti-fibrinogen. A range of voltages was tested to optimize removal efficiency for of the non-specific biomolecules. This non-contact system can remove non-specific or specifically bound molecules from the surface.

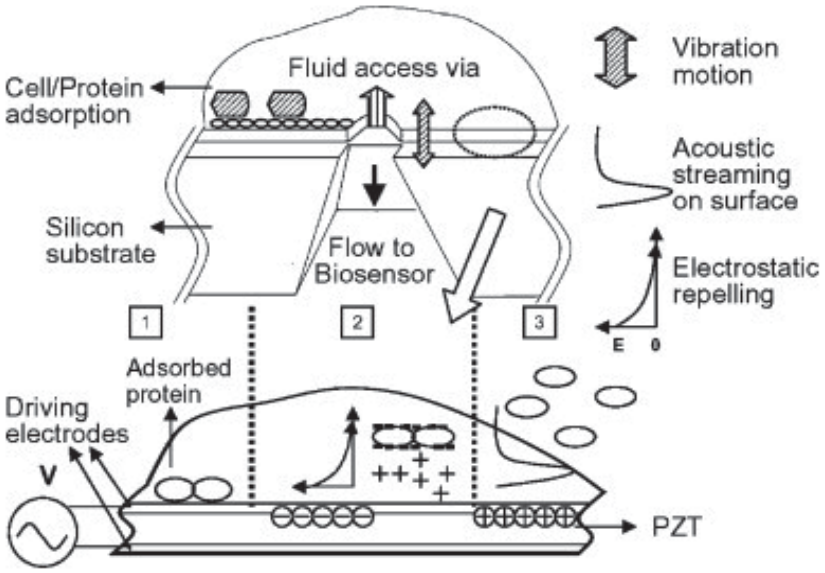

Figure 2.4. Schematic diagram of the piezoelectric membrane as an implantable sensor coating. The membrane is composed of two driving electrodes with a piezoelectric material in between. Adsorbed proteins can be desorbed by an electric field and carried away by acoustic streaming generated by the vibration. Reprinted from Ref. [74] with permission from Elsevier.

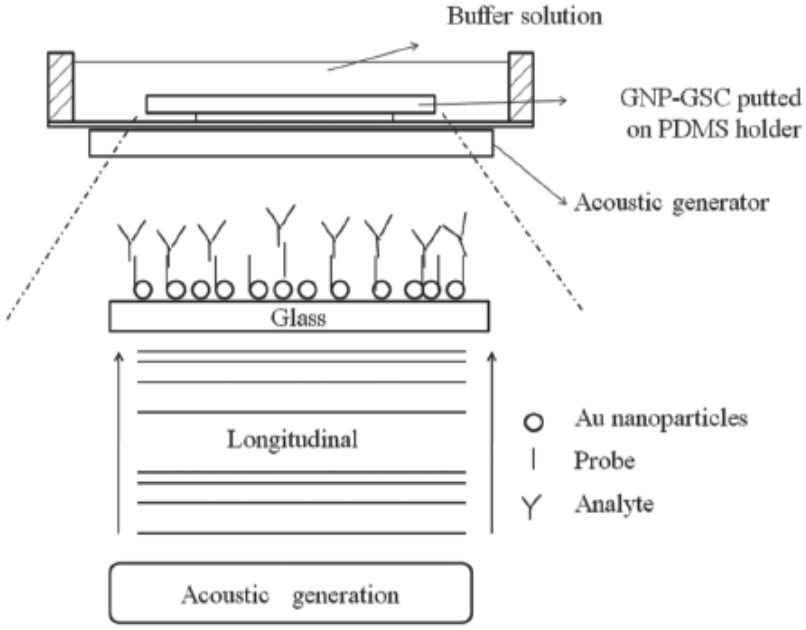

Figure 2.5. Schematic representation and working principle of the experimental setup for generating LAWs and transmitting to a GNP-GSC through buffer solution. Biomolecular binding at the surface of the functionalized GNPs removed by the acoustic wave effect. Reproduced from Ref. [90] with permission from The Royal Society of Chemistry.

Fluid-based. Fluid-based methods of NSA removal utilize the pressure-driven flow already integral in microfluidic lab-on-chip systems to remove NSA on the sensing surface along the bottom channel wall (Fig. 2.6). Other applications of fluid manipulation in channels includes the use of hydrodynamic forces to manipulate membrane-bound proteins in a cell membrane [109] and for polystyrene sphere removal on quartz surfaces [110], [111]. Another example is using a confining sheath fluid within a microfluidic channel to prevent NSA [112]. However, this method is limited in scope to adsorption-free T-sensor measurements to be made within the core of the flow channel [112] and is not applicable for surface-based sensing.

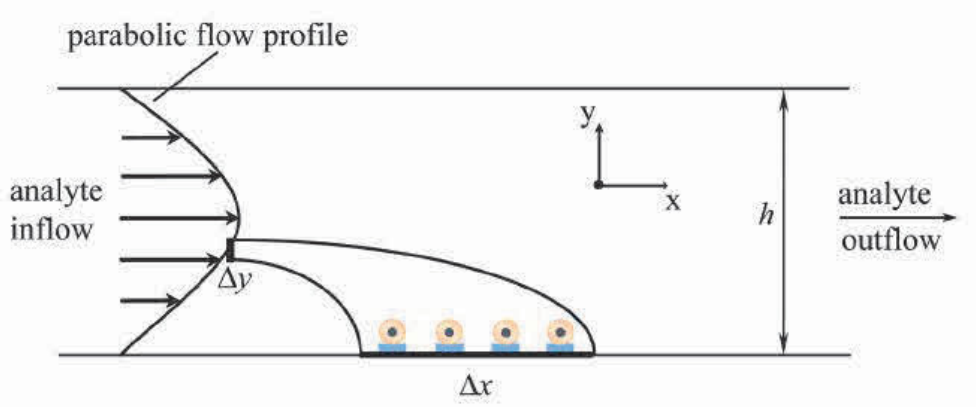

Figure 2.6. Diagram of how pressure-driven flow creates a parabolic velocity profile, which can behaves on immobilized bioreceptors and bound analytes in microchannel. Reproduced from Ref. [97] with permission of AIP Publishing.

Hydrodynamic shearing is a transducer-free method of non-specific binding removal, not commonly found in literature. Li *et al*. applied this technique to effectively remove non-specifically bound carbon nanotubes (CNT) on a multiplexible biosensor after electrophoresis alignment using a 1X PBS solution shearing at 500 μL/min (Fig. 2.7) [93]. The CNTs bridge across the two parallel electrodes to bind with targets. Due to the large hydrodynamic drag imposed by the cross-flow of the cylindrical CNTs with

high aspect ratio, a critical hydrodynamic shear rate removed the non-target linkers of the aligned CNTs. Detection limits of 100 aM and 10 fM in pure samples for two ELISA tests: biotin/streptavidin and HER2 (Human epidermal growth factor receptor 2) /HER2 antibody were achieved. For both models, the dynamic range was tuned up to five orders of magnitude by increasing the CNT numbers, with high sensitivity and specificity. The researchers used biotin-streptavidin as the antigen-antibody pair to optimize the flow rate [93]. The key step in this process is the DC electrophoresis and AC dielectrophoresis to align the CNTs before shearing. This requires gold electrodes fabricated into the device and additional time (20 min) for the CNTs assembly [93]. This system is proposed as an improved sensitivity ELISA assay, with a cost estimate of $20 USD per test.

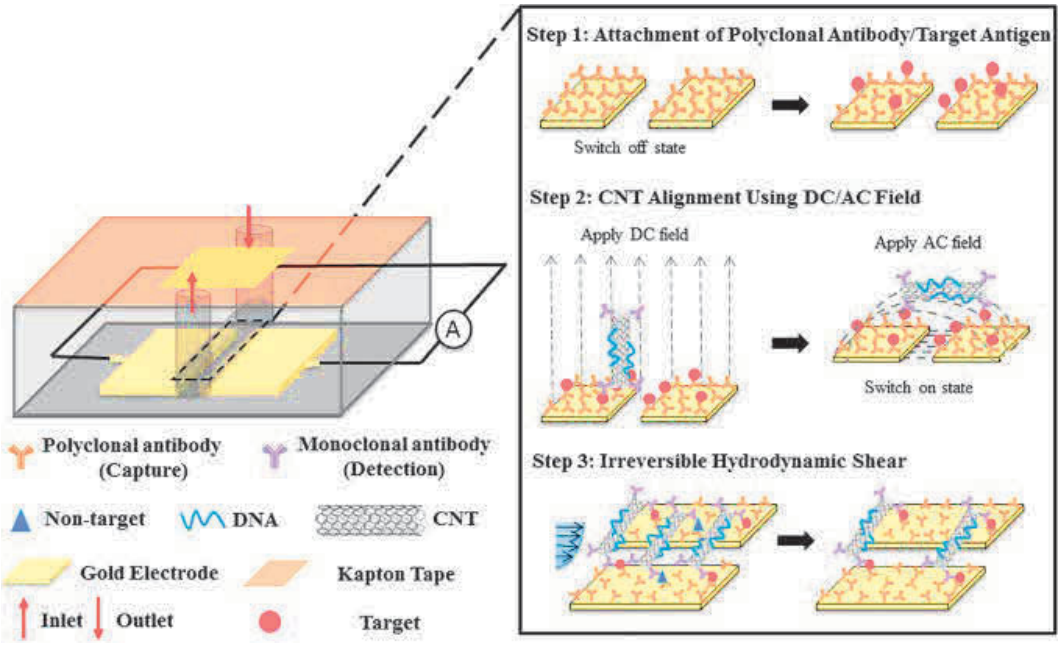

Figure 2.7. Schematic of CNTs switch sensor for protein detection. Reproduced from Ref. [93] with permission of Elsevier.

Discussion

In summarizing the various methods of NSA reduction in sensing, the main disadvantage of the passive methods is their inconsistency and tedious processes required. The main disadvantage of the transducer methods is that they require extra and equipment. The main disadvantage of the fluid-based methods is the precise fluid manipulation. Ultimately, there is not a single ideal method of NSA reduction for all sensors. However, we suggest the optimal method to be chosen based on several factors: (1) Integration, (2) Multiplexibility, and (3) Tunability. First, the method of NSA reduction should be easily incorporated with the existing sensor structure. Note that many of the active removal methods are designed for microfluidic devices [36] while the passive methods could be applied to most surface-based sensors. Second, the method ideally can be applied to different sensing areas, since most sensors have or strive to have multiplexibility. Third, the method should be able to be adjusted for different experimental conditions, i.e. analyte/receptor combinations or device size. Other factors like ease of operation, and cost will play a role too.

When comparing biosensor performance, it is important to recognize the sensitivity depends on the analyte, recognition molecule, and surface immobilization method used [94]. The non-specific adsorption is highly dependent on all of those things, and repeatable results are of course necessary for successful demonstration of a NSA reduction method. Also, the authors point out one key limitation to measuring the efficiency of NSA removal methods is how researchers evaluate their devices' anti-fouling ability. The most common method for evaluating adsorption is to compare the residual material left on the device after a typical use [113]. While this is direct and

simple, it ignores transient adsorption [113]. Hawkins *et al.* present a solution to this issue, developing a microfluidic device for transient monitoring of adsorption [113].

Non-specific adsorption is a critical problem in biosensing. While various methods exist to reconcile the problem, none of them are sufficient to create an ideal biosensor. In this review, we discussed the various passive and active methods of NSA reduction for biosensors. There is a trend present in the past decade of transitioning from surface chemistry NSA prevention to actively removing using transducer-based or fluid-based methods. A comprehensive table summarizing the reported methods of active NSA removal in biosensing and criteria for choosing a method of NSA reduction was given. Despite the extensive published literature, several important areas remain relatively unexplored. The first is investigating the use of various bioreceptor–analyte combinations in conjunction with transducer-based active NSA methods. The second is the ability of the NSA reduction method to not only limit NSA, but also improve specific binding, which a few studies claim. The last is combining active and passive NSA reduction methods in hopes of achieving further improved sensitivity. The research on methods to combat non-specific adsorption will likely continue to grow with the ever-expanding field of biosensor development and the increase in miniaturization technologies. With the shift from passive methods to active removal methods, the ability to use the more complex methods of NSA removal for a multitude of sensor types should be explored further.

CHAPTER THREE

Investigation of a Trapezoidal Microchannel for Hydrodynamic Detachment

As a solution to the limitations of existing microfluidic shear generating methods discussed in Chapters One and Two, a trapezoidal microchannel design is proposed (Fig. 3.1) with a narrower channel height at the region of interest (ROI) in the center of the channel (ie. sensing area, detachment area) to achieve a higher shear stress. Here, we will detail our calculations and simulations to investigate the feasibility and limitations of this design.

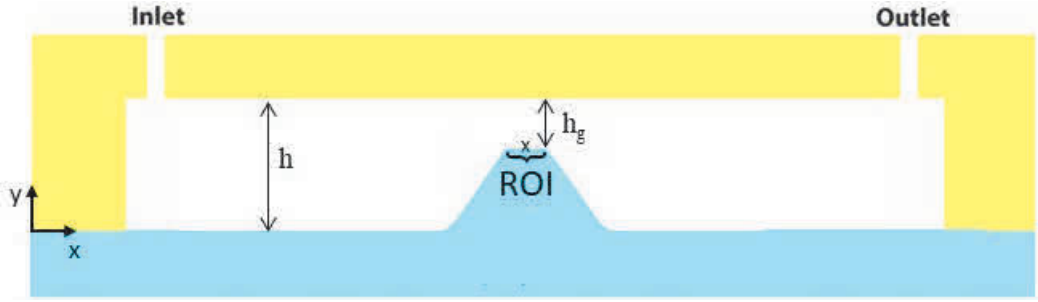

Figure 3.1. Schematic of trapezoidal microchannel in the x-y axis, with the ROI in the center of the channel where the channel height is reduced. The channel height, h, and gap height, h_g, are denoted. The "x" in the center of the channel marks where the wall shear stress is calculated in this study.

Theory

The solutions to the governing equations of fluid motion, the Navier-Stokes and continuity equations, provide the fully developed velocity profile across the cross-section of a microfluidic channel (Fig. 3.2). An object experiences shear stress when a tangential

force is applied to its surface [114]. In fluids, the shear stress throughout a channel can be represented mathematically with Newton's law of viscosity,

$$\tau = \eta \frac{\partial U}{\partial y}, \tag{3.1}$$

where τ is the shear stress, η is the fluid viscosity, U is the fluid velocity, and y is the position within the channel (Fig. 3.2). This derivative of the velocity with respect to position y is evaluated at $y = 0$ to provide the wall shear stress [115],

$$\tau_w = \eta \frac{\partial U}{\partial y}\Big|_{y=0} \Rightarrow \frac{6\eta U}{h}, \tag{3.2}$$

*w*here h is the channel height. This equation is for steady flow between infinitely wide parallel plates.

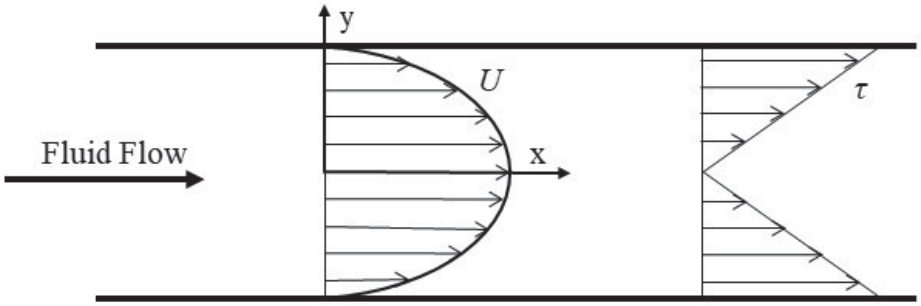

Figure 3.2. Velocity and shear stress profiles of fluid flow in a microchannel with rectangular cross-section ($L >> w >> h$).

The pressure drop, ΔP, in a microchannel is directly proportional to the flow rate, Q, and channel length, L. The relationship for pressure gradient is given below:

$$\frac{\Delta P}{L} = -\frac{12\eta Q}{wh^3} \tag{3.3}$$

The pressure drop increases with frictional shear forces in microchannels. Physical properties such as surface roughness, convergence, divergence and turns can affect the pressure drop.

Equation 3.2 was used to create a map of wall shear stress in channels with different flow rates (Fig. 3.3.a). The fluid viscosity of water was used (η = 0.89 mPa·s), which is similar to the viscosity of phosphate buffered saline (PBS), a commonly used buffer solution in microfluidic applications. In Fig. 3.3, for the ranges shown, it is clear that changing the channel height affects the wall shear stress more than changing the flow rate.

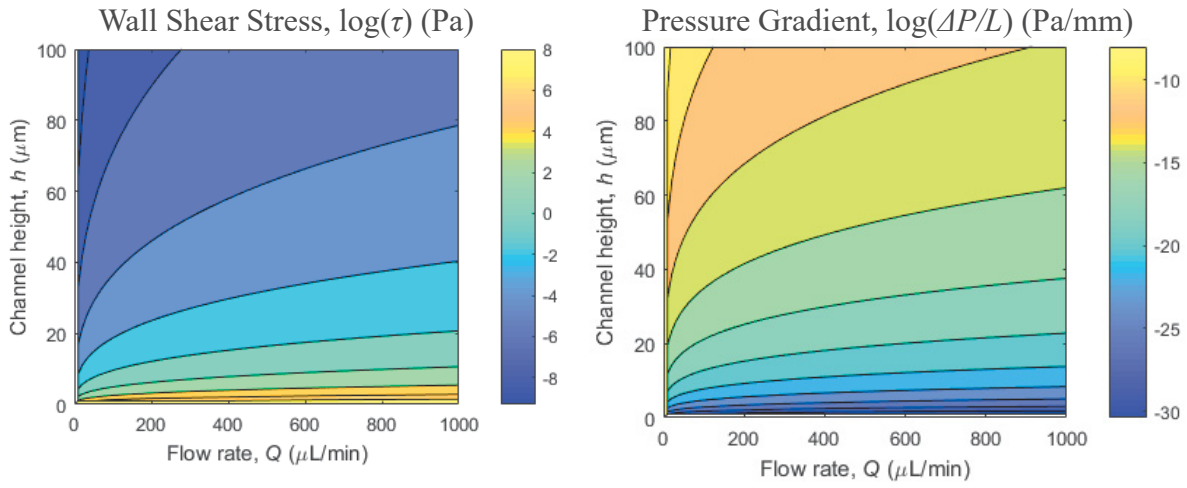

(a) (b)

Figure 3.3. Contour plot of (a) log scale wall shear stress (Pa) and (b) log scale pressure gradient (Pa/m) produced by different channel heights over a range of flow rates. The aspect ratio is fixed where *w* is 10 times larger than *h*.

In order to produce larger stresses on cells or biomolecules in hydrodynamic flow experiments, the wall shear stress must be increased while ensuring that the flow remains laminar [4]. One method to accomplish laminar flow is to reduce the channel height, which introduces the use of microfluidics [4]. Laminar flow is characteristic of microchannels due to the low Reynolds number (*Re*) [6], where the Reynolds number is the relation of viscous to inertial forces and is defined as

$$Re = \frac{\rho \bar{U} h}{\eta}, \tag{3.4}$$

where channel height, h, is the characteristic dimension. Microfluidics for cell detachment has the advantages of straightforward construction and operation; real-time observation and measurement; compatibility with cell sizes; fast and simple operation; and non-invasiveness to cells [1]. Because of the small dimensions, it is possible to achieve large shear stress while preserving laminar flow [4], [116]. Based on Eq. (3.1), for a given maximum fluid velocity the shear stresses present in a smaller microchannel are greater than those in a larger microchannel [114]. At a given flow rate, the smaller channel height (along y axis) and width (along z axis), the higher the wall shear rate [6]. In microfluidics, the finite width generates a parabolic fluid velocity profile between the plates, but vanishes at the boundaries of the rectangular channel. The shear stress profile, calculated from the velocity gradient Eq. 3.1 has maximum magnitudes at the plate surfaces and vanishes at the corners of the channel [117]. One can assume constant shear stress across the width of the channel, except for near the corners, where it drops to zero.

Miniaturizing microfluidics affects the most significant performance metrics of biosensors: response time and limit of detection [16]. Nanoscale dimensions in sensors enhances the signal-to-noise ratio by increasing the signal density and decreasing background signals [16]. However, the improved limit of detection can be a trade-off for the longer time for the target analytes to collect on sensor surfaces due to increased mass transport times [16].

Many studies have focused on theoretical models and experimental demonstration for cell detachment under a shearing flow [115], [118]–[120]. Gaver and Kute demonstrated the fluid shear stress on a cell is equal to the shear stress at the wall for *R/h*

< 0.25 where R is the cell diameter and h is the height of the microchannel [118]. Couzon *et al* furthered this work by using the findings from Gaver and Kute to develop an equation for critical wall shear stress (τ_C) or the shear stress needed to remove an adhered cell to a channel wall,

$$\tau_C = N f_{ad_z} \frac{1}{4R^2} \frac{\left(1 - \left(\frac{R}{h}\right)^2\right)^{\frac{5}{2}}}{3.19 + 0.65\frac{R}{h} + 4.34\left(\frac{R}{h}\right)^2}, \tag{3.5}$$

where f_{ad_z} is the force of each focal adhesion site on the cell in the direction of flow, and N is the number of focal adhesion sites. For small channels (h < 100 μm), the τ_C increases rapidly with h. The increase for higher channels is much slower and plateaus when h becomes large. Therefore, the simplified equation can be used in such cases,

$$\tau_C = \frac{N f_{ad_z}}{12.76\, R^2} \tag{3.6}$$

These equations were used to estimate the forces developed at each focal adhesion site of cancer cells adhered to a microchannels of varying heights [115]. They used R, cell diameter, = 15 μm with channel heights from 60-260 μm, widths of 1 mm and found a τ_c = 5 Pa. The authors found their results to be similar to available or estimated values of cell adhesion for different cell types. These values were used in this study, defining the critical shear stress to be 5 Pa, based on a total binding force of 12 nN for a T24 cell. The ability to achieve high shear stresses are vital when considering how the stress, force and torque can vary based on channel dimensions and cell type [118].

Based on Eq. 3.6 and the data in Couzon *et al.,* a formula was created to determine the channel height necessary to detach a cell with certain diameter, R, and total binding force, NF_{ad}. This critical channel height, h_c, is defined below.

$$h_C = \sqrt{\frac{76.56R^2\eta Q}{f_{ad_z} w}} \tag{3.7}$$

This equation was used to create a plot (Fig. 4) based on the R and NF_{ad}, where a constant Q/w = 2.34 x 10^{-6} m^2/s and N = 40 was used. This plot demonstrates a small h_c is needed to overcome the range of total binding forces, for most of the cell diameter values.

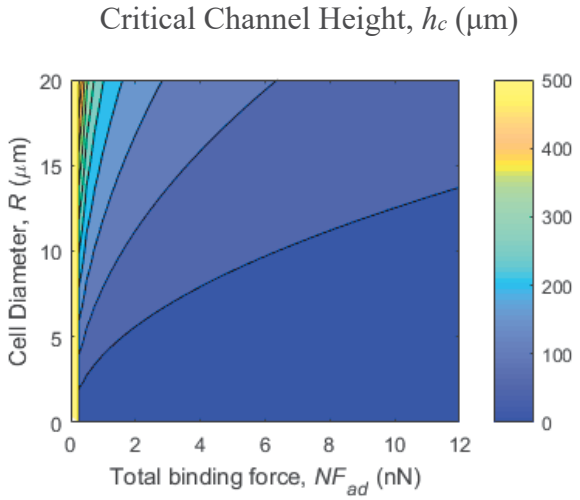

Figure 3.4. Contour plot of the critical channel height needed for a given cell diameter and adhesion force, based on experimental and literature data in Couzon *et al*. A constant Q/w = 2.34 x 10^{-6} m^2/s and N = 40 are used.

This can be applied for other cell detachment studies, and it is hypothesized it can also be applied to the removal of biomolecules, such as proteins, to reduce NSA. For example, biotin and streptavidin are known to have a strong binding affinity and are commonly used for protein assays. Biotin and streptavidin are known to have high affinity for each other. Biotin is a water-soluble B vitamin. Streptavidin is a 52.8 kDa protein obtained from the bacterium *Streptomyces avidinii*. The binding of biotin and streptavidin is commonly used as the target biomolecular interaction in biosensors and

cell sorting because it is one of the strongest non-covalent interactions in nature with an affinity constant of 10^{15} L/mol [121]. Additionally, the binding is not affected by changes in pH or multiple washes. Streptavidin is commonly used rather than avidin because of its advantage of lower nonspecific binding. With biotinylated BSA as the analyte and streptavidin as the bioreceptor, the adhesive force is about 250 pN across literature [81], [122], [123]. The non-specific binding force can be estimated to be about 50% of the adhesive force, or 125 pN. The N would be the number of biotin – streptavidin bonds, which could be estimated based on the functionalization area. The diameter of a protein is several order of magnitudes of smaller than a cell, with proteins being a just few nanometers in diameter, e.g. BSA is 4 nm x 4 nm x 14 nm and streptavidin is 5.6 nm x 4.2 nm x 4.2 nm. The critical wall shear stress equation could be used to determine the necessary flow rate for the estimated detachment of weakly adsorbed proteins. However, because this is based on a cell model, the τ_c would likely be an overestimation for protein detachment, due to the simpler nature of protein attachment compared to cell attachment.

Straight Microchannel

The wall shear stress (Eq. 3.2), pressure drop (Eq. 3.3), and Reynolds number (Eq. 3.4) were analytically calculated for straight microchannels with h = 50 μm and 500 μm (Case A and B of Table 3.1), with a width 10x greater than the h, and L = 1 cm. The 2D flow rate is was kept constant where Q/w = 2.34 x 10^{-6} m^2/s, defined to achieve a τ_w = 5 Pa in Case A to match the τ_c = 5 Pa in Ref. [115]. The channel dimensions are based on commonly used microfluidic channels in literature for cell detachment studies [5], [93], [114], [115]. The objective was to demonstrate the different shear stress and pressure drop produced in the channels due to their different heights.

The results from the analytical calculations of the straight microchannels with h = 50 μm and 500 μm demonstrate the τ_w produced by channel A is 5 Pa as expected, and 0.05 Pa for channel B. The ΔP is different by three orders of magnitude (Table 3.1) for Case A (2000 Pa) and B (2 Pa). Pressure is an important consideration in microfluidics because high pressure build-up can lead to the deformation or delamination of the microchannels, which are commonly fabricated using soft lithography or photolithography [124]. The Reynolds number is calculated to ensure laminar flow (Re < 2300), using h as the characteristic dimension. For both channel A and B, Re = 2.62, which is reasonable for microfluidics.

One disadvantage of a miniaturized channel is increased flow time required for a specific sample volume. For example, for a diagnostic biosensor using a blood as the biological sample, the average amount of serum from a single drop of blood is 5 - 12.5 μL. In the channel in Case A (h = 50 μm) with a w = 500 μm, the total volume of the microchannel is only 0.25 μL. However, for channel B (h = 500 μm), the fluid volume is 25 μL, 100 times greater. One solution to increase the volume of channel A is to increase the channel length. However, that could significantly magnify the pressure drop, which can be risky as previously discussed. Another solution to overcome this limitation is using parallelization, where several channels in parallel allows for a greater throughput. However, parallelization can add additional fabrication.

Trapezoidal Microchannel

A trapezoidal microchannel (Fig. 3.1) is a potential alternative to these issues. By having a channel with a reduced height at the ROI, a higher shear stress can be achieved while maintaining the benefits of a larger microchannel. It is anticipated the larger

channel volume on the sides of the trapezoidal structure allow for a greater sample volume to be held, while conserving a modest pressure drop. We expect this trapezoidal channel design may be applied for applications other than cell adhesion studies, such as biosensing. Perhaps, a microfluidic shear assay with a nanoscale trapezoidal area can be used in the hydrodynamic removal of non-specifically adsorbed proteins in biosensing applications, where the proteins have a diameter of less than 1 μm.

For the fluid dynamics evaluation of the trapezoidal channel, computational fluid dynamic (CFD) simulations were employed. Two trapezoidal channels were simulated (Channel E and F in Table 3.1) with h = 500 μm and gap height (h_g) = 50 μm. For the fluid dynamics evaluation of the trapezoidal channel, computational fluid dynamic (CFD) simulations were employed. Two trapezoidal channels were simulated (Channel E and F in Table 1) with h = 500 μm and gap height (h_g) = 50 μm. To ensure the the flow was fully developed at the center of the channel, the entrance length (L_e) of Channels A and B were calculated using the equation,

$$L_e \approx 0.05(Re)(h). \tag{3.8}$$

The entrance length is the channel position at which the boundary layers meet, and the flow after this point is fully developed. The velocity distribution across the channel cross section will no longer change, but remains steady along the channel length [6]. The entrance length was calculated to be 65.5 μm for Channel A (h = 50 μm) and 655 μm for Channel B (h = 500 μm). The length of the trapezoidal flat surface should be greater than 65.5 μm to ensure fully developed flow.

The trapezoidal microchannel was optimized to minimize pressure loss. A trapezoidal channel with sloped sides and a flat top surface (red dashed line in Fig. 3.5)

was first investigated. However, the pressure drop for that channel was 372 Pa. With the goal of reducing pressure loss due to the sharp corners, a hyperbolic tangent function was used instead to create a smoother trapezoidal structure (Fig. 3.5). The width of the hyperbolic tangent ($\boldsymbol{\ell}$) was varied, while the $L_{T,2}$ was kept constant at 2 mm and $\boldsymbol{\ell} = \boldsymbol{\ell}^*$. The results show the pressure drop decreases with increasing $\boldsymbol{\ell}$ (Fig. 3.6a). However, a longer $\boldsymbol{\ell}$ will reduce the channel volume. A $\boldsymbol{\ell}$ = 400 μm was used to test different L_T values, where the L_T is the top surface of the trapezoidal structure and could vary depending on the specific detachment application. The results show the pressure drop increases proportionally to the L_T (Fig. 3.6b). From these results, two different L_T cases were compared to the straight microchannels (C and D). Channel E has an L_T = 0.5 mm and Channel F has an L_T = 2.5 mm. The shear stress at the center of the bottom wall of the channel at the ROI was calculated using Eq. (3.1). The pressure drop was found using the relationship: $\Delta P = P_{inlet} - P_{outlet}$. The volumes of the two proposed trapezoidal channels were calculated in the same way as the straight channels, assuming the width is 10x the height.

The results for the analytical calculations and simulations are displayed in Table 3.1. Velocity plots from the CFD simulation results are shown in Fig. 7b for Channels C – F. The simulated straight channels have a similar shear stress (C: τ_w = 4.98 Pa, D: τ_w = 0.049) and pressure gradient (C: ΔP = 1999 Pa, D: ΔP = 1.98 Pa) to the analytical calculations (A: τ_w = 5 Pa and ΔP = 2000 Pa, B: τ_w = 0.05 Pa and ΔP = 2 Pa). The trapezoidal channels (E and F) produced similar very wall shear stresses (4.96 Pa) and with lower pressure drops (259 Pa in Channel E and 589 Pa in Channel F) compared to Channel C. By using the same flow rate in all the channel cases, the expectation was to

achieve the τ_c = 5 Pa at the ROI of the trapezoidal channels, similarly to the straight microchannel in case A and C. The simulations show the wall shear stress in Channel E is 99.5% of the wall shear stress in Channel C with 13% of the pressure drop. The wall shear stress in Channel F is the same as Channel E, with 29% of the pressure drop of Channel C. As expected, for both trapezoidal cases, a wall shear stress similar to Channel C is achieved with a fraction of the pressure drop. Channel E and F has similar shear stress, likely due to fully developed flow profile at the center of the L_T. Additionally, the fluid volumes of the trapezoidal microchannels (E: 21.8 µL and F: 19.8 µL) are similar to Channels B and D with a larger channel height (25 µL) and are 90x and 80x greater than the volume of Channel C (0.25 µL). The reduced channel height at the ROI does not limit the volume capability of the trapezoidal microchannels.

Table 3.1. Microfluidic fluid dynamics results for two analytical cases (A and B), and four simulated cases (C - F), where A - D are straight microchannels and E - F are trapezoidal microchannels. A constant Q/w = 2.34 x 10^{-6} m^2/s and L = 1 cm is used.

Variable	Analytical		Simulated				Units
Channel	A	B	C	D	E	F	
h	50	500	50	500	500	500	µm
h_g	-	-	-	-	50	50	µm
L_T	-	-	-	-	0.5	2.5	mm
U	46.8	4.68	46.8	4.68	4.68	4.68	mm/s
τ_w	5	0.05	4.98	0.049	4.96	4.96	Pa
ΔP	2000	2	1999	1.98	259	589	Pa
V	0.25	25	0.25	25	21.8	19.8	µL

The ability to generate a high critical wall shear stress with lowered pressure drop is a clear benefit to this design. Additionally, the isolation of the reduced height area to just the ROI allows for flexibility in the rest of the channel to incorporate other microfluidic components, and hold a larger fluid volume without parallelization. These outcomes of this study demonstrate the potential of this trapezoidal microchannel design to achieve a critical wall shear stress in microfluidic applications such as cell detachment or protein NSA removal.

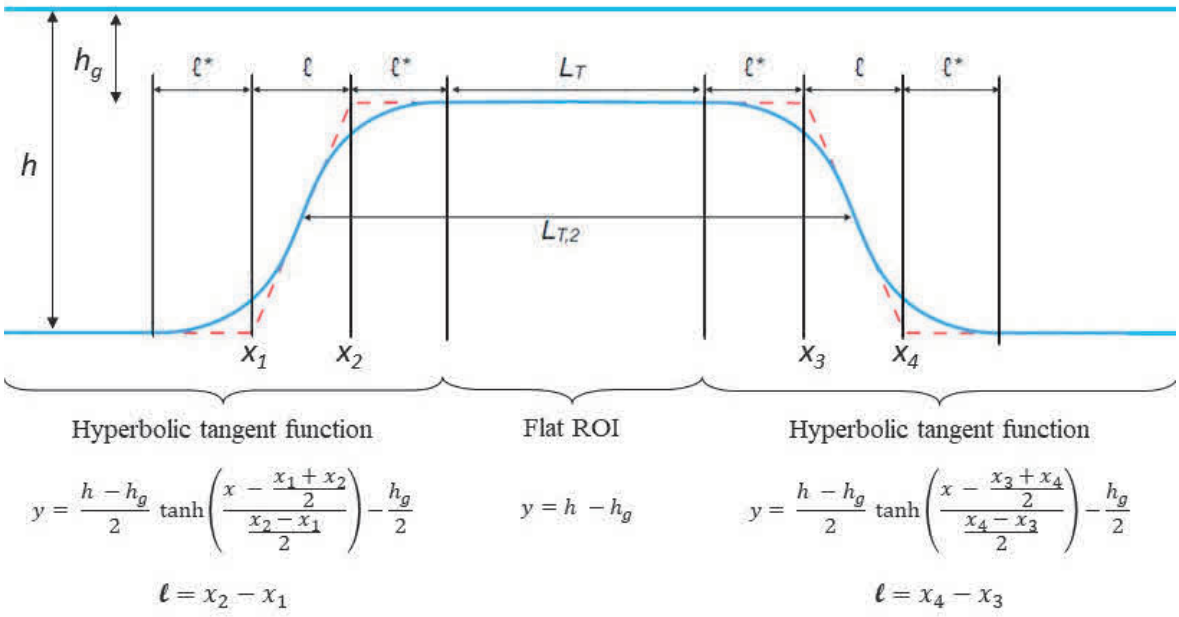

Figure 3.6. Schematic of the trapezoidal channel geometry. The blue lines denote the channel wall, and key dimensions are labeled. The equations used to create the smooth channel surfaces are detailed for each part of the trapezoid.

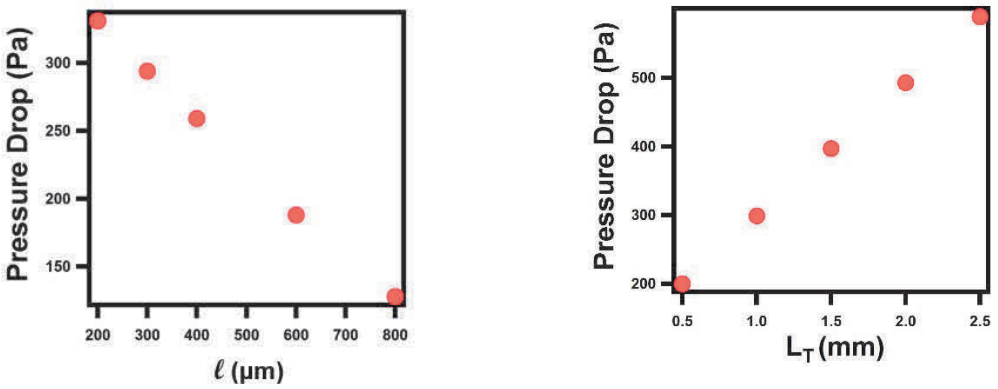

Figure 3.7. The pressure drop as a function of (a) ℓ and (b) L_T.

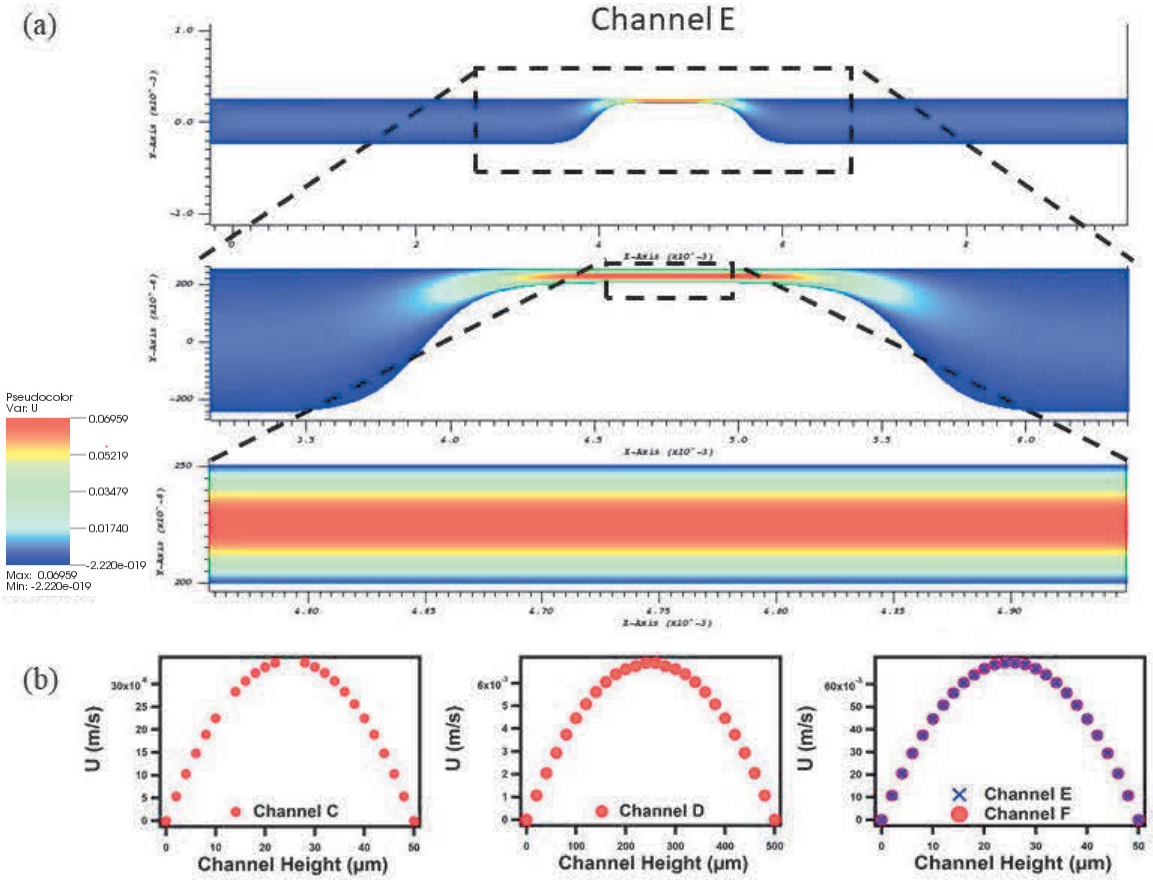

Figure 3.8. (a) CFD simulation color plot of the velocity in Channel E, with a close up of the center of the channel. (b) Plots of the velocity profiles for all 4 simulations. The velocity profile of the trapezoidal matches that of the straight channel cases.

CHAPTER FOUR

Preliminary Fabrication and Functionalization

3D Printed Trapezoidal Microchannels

Three-dimensional (3D) printing has revolutionized the research and engineering fields since its beginning about 40 years ago. In recent years, the use of 3D printing has expanded greatly and evolved to the application of microfluidics. Compared to traditional microfabrication methods, the advantages include reduced cost, space, and equipment [125]; being a one-step process; easy integration of electrodes, connection ports, or complex flow regulating components; enhanced multiplexability, versatility, and reusability [126]; and ability to achieve complicated structures [126], [127]. Adjustments to a design can be easily modified in a design program (e.g. AutoCAD) [126], and replicating devices is easily performed with the automated machine [126].

However, there are some limitations, including resolution, surface properties, compatibility, transparency, and gas permeability [126]. While printing resolution can vary based on the printer, materials, and method used, stereolithography (SL) has demonstrated high printing resolution adequate for microchannels (25 μm wide channel) [128]. SL has been demonstrated as a feasible rapid prototyping method to print transparent biocompatible polymers for microfluidic applications [129]. This technique operates by producing 3D polymer structures from a liquid photopolymer resin with a focused laser or LED light source [129]. The laser beam diameter and resin determine the print resolution [129]. One disadvantage of this process is that the uncured photopolymer

precursor must be drained after printing [129]. Over-curing can create unwanted roughness in the channels [129].

To fabricate the trapezoidal microchannel investigated here, a Digital Light Processing (DLP) 3D printer (B9Creator v.1.2, B9Creations, Rapid City, SD, USA) was employed. A DLP printer uses liquid photosensitive resin in a vat with an inverted stage. The printer exposes the entire layer at once using a beam projector under the resin vat to print an object layer by layer, which makes it faster than SL printing. This type of printer was chosen due to the improved resolution, and printing speed compared to other 3D printer types (e.g. fused deposition modeling, polyjet) [130]. The x-y resolution can be set to 30, 50, or 70 μm and the z resolution is dependent on the specific resin used in printing. Two resins were evaluated, a yellow casting resin (z resolution: 20 μm) and black prototyping resin (z resolution: 30 μm) to determine the print quality for the trapezoidal structure. A trapezoidal channel was designed with three trapezoidal elevations and base lengths. SEM micrographs were taken of the printed designs (Figure 4.1a), measurements of the printed features were recorded for three prints (Table 4.1), and the surface roughness was evaluated using an AFM (Figure 4.1b).

For the black resin, the printed width and elevation were more accurate than the yellow. For the yellow resin, the trapezoidal base lengths were similar to the desired lengths, but the elevations were about half of the expected. The surface roughness R_q and R_a values are similar for both resins. In comparing the overall print results for the two resins, the black resin was more accurate in printing the desired feature sizes, with similar roughness properties.

Table 4.1. 3D print measurements for two resins, with a designed base length of 1,200 µm and width of 500 µm. (n = 3, mean ± std dev)

Resin	Desired Elevation	Base	Width	Measured Elevation
B9R-4-YELLOW	200	1135 ± 311	526 ± 21	106 ± 56
	400	1123 ± 499	533 ± 38	190 ± 136
	600	1135 ± 510	531 ± 30	248 ± 186
B9R-2-BLACK	200	1017 ± 52	497 ± 68	164 ± 14
	400	1098 ± 68	516 ± 52	333 ± 10
	600	1144 ± 57	516 ± 51	498 ± 12

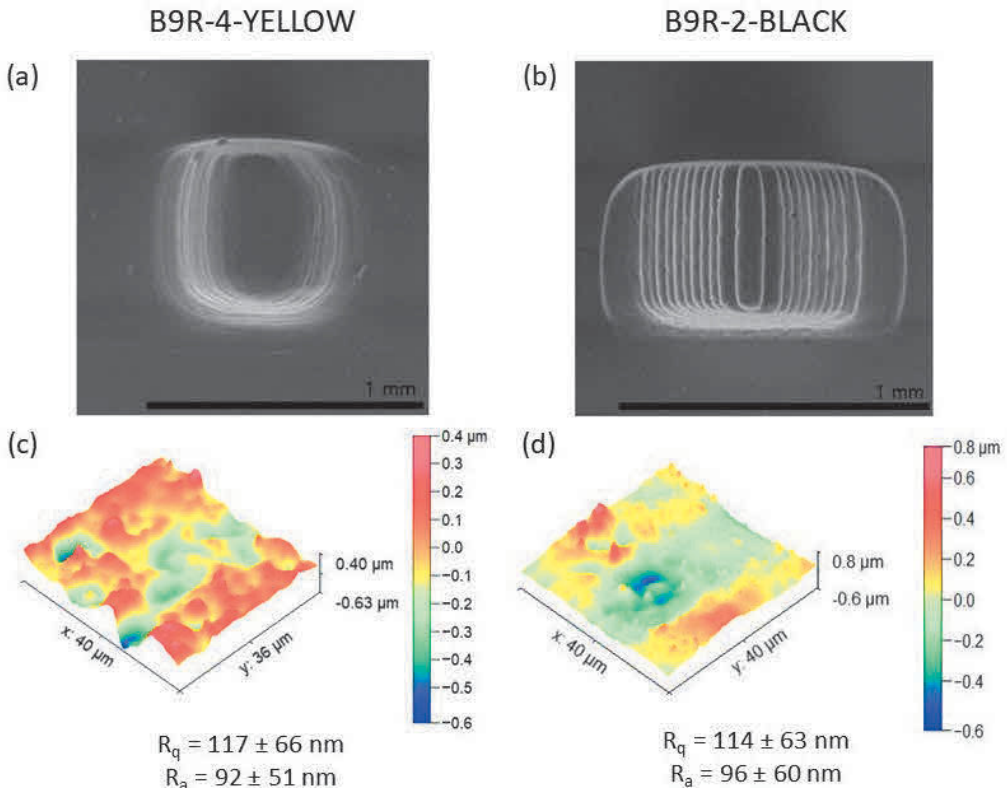

Figure 4.1. Resin analysis for B9R-4-YELLOW (a, c) and B9R-2-BLACK (b, d). (a) and (B) are SEM micrographs of the 3D printed trapezoidal structures (top view). Note the definite layers produced with the black resin. (c) and (d) are 3D surface roughness plots for 40 µm x 40 µm area with n = 3 for mean ± standard deviation. R_q is the root mean squared roughness and R_a is the arithmetic average roughness.

The black resin should produce 6, 13, and 20 layers for the designed elevations 200, 400, and 600 μm. The yellow resin should produce 10, 20, 30 layers for the same elevations. The number of layers can be clearly seen and counted for the black resin (Fig. 4.1b), but the layers are not clearly defined for the yellow resin (Fig. 4.1a). The difference in print accuracy might be due to the transparency of the yellow resin compared to the opacity of the black resin. Because projector light is used to cure each layer, the transparent resin may not cure the same as an opaque resin, which can affect the print accuracy. Additionally, variables such as room temperature and resin age can affect the fabrication of DLP or SLA printing [130].

Surface Functionalization

In order to demonstrate the detachment ability of this design, preliminary surface functionalization protocols were established for protein NSA removal. Biotin and streptavidin are used, with the benefits of this interaction described previously in Chapter Three. The tetrameric structure of streptavidin enables four binding sites for biotins (Fig. 4.2).

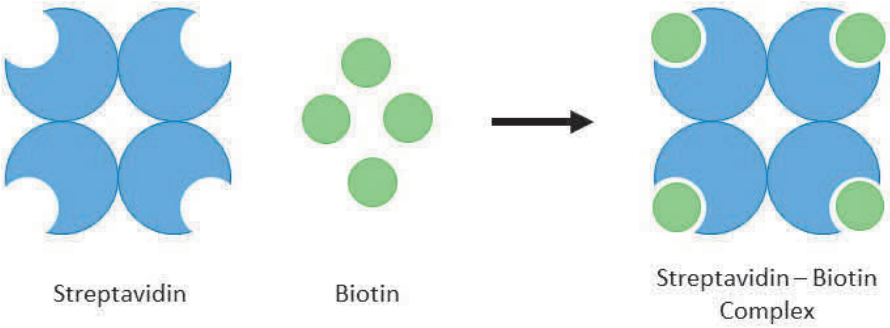

Figure 4.2. Schematic of the binding of biotin and streptavidin.

Surface chemistry was employed to immobilize the streptavidin to the glass substrate. The amine groups of the streptavidin bond electrostatically to the (3-Aminopropyl)triethoxysilane (APTES) surface. The binding of the biotin to the streptavidin is verified through fluorescence microscopy using fluorescein conjugate biotin. Fluorescein is a yellow water-soluble dibasic dye, commonly used fluorophore in microscopy, and has an absorption maximum of 494 nm and an emission maximum of 512 nm (in water).

The biological preparations were performed prior to functionalization. Phosphate buffered solution (PBS) used in the solutions is 1X dilution and pH 7.4. APTES or (3-Aminopropyl)triethoxysilane was prepared as a 5% solution in DI water. Streptavidin was prepared by mixing 0.5 mg with 0.5 mL of DI water, and then 16 mL of PBS to form a 30 μg/mL concentration. Fluorescein conjugate biotin was prepared by mixing 1 mg of biotin with 0.2 mL of Dimethyl Sulfoxide (DMSO) (Thermo Fisher Scientific, Waltham, MA, USA) and 0.8 mL of PBS to form a 1 mg/mL concentration. This was mixed with 99 mL of PBS to create a 10 μg/mL solution. One mL of 10% BSA in PBS was mixed with 10 mL of PBS to create a 1% solution. All protein solutions were stored at 4°C in dark containers until used. Standard glass microscope slides were used for all experiments (75 mm x 25 mm), and are referred to as the substrate in subsequent text.

The detailed procedure for surface functionalization is described below and depicted in Fig. 4.3.A - B.

1. Clean the substrate with DI water and IPA as needed. Dry with nitrogen gas stream.
2. Expose to oxygen plasma for 1 minute to activate the hydroxyl groups on the surface.

3. Apply 5% APTES solution to cover the surface and incubate in enclosed space for 30 min.

4. Thoroughly rinse substrate with DI water to remove any unbound silane groups and dry with nitrogen.

5. Place substrate on hot plate for 10 minutes at 110℃ to anneal APTES.

6. Let substrate cool down to room temperature to prevent denaturation of streptavidin.

7. Mix streptavidin with orbital shaker for 30 seconds at 140 rpm.

8. Use permanent marker to define functionalization areas. Apply streptavidin to desired areas on substrate and incubate for 1 hour in enclosed space.

9. Rinse with DI water and dry with compressed air.

10. Mix fluorescent biotin with orbital shaker for 30 seconds at 140 rpm.

11. Pattern fluorescent biotin onto substrate and incubate for 1 hour in dark enclosure to prevent photobleaching.

12. Rinse with DI water and dry with compressed air.

13. Inspection using fluorescence microscopy

An Olympus BX51 microscope was used for fluorescence microscopy. The images were captured with Infinity Analyze and Capture program (Teledyne Lumenera, Ottawa, ON, CA) with the a 190 ms exposure time and 10x magnification. The images were processed using ImageJ, an image processing program, to measure the mean intensity of the pixels. The intensity values were normalized with the baseline fluorescence of the background and are displayed in Figure 4.3c.

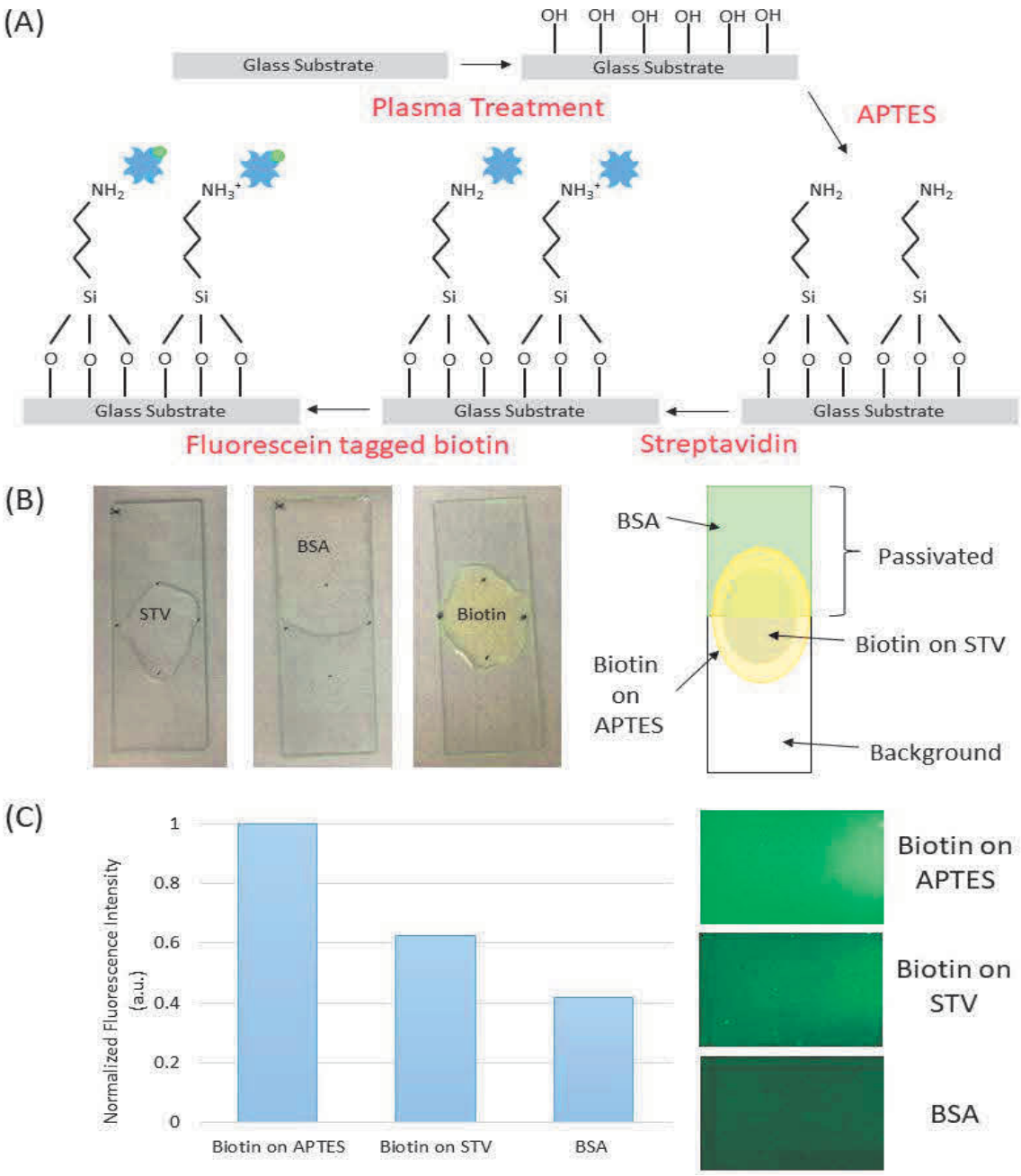

Figure 4.3. Surface functionalization and fluorescence microscopy (A) Procedure used to immobilize streptavidin and detect fluorescein tagged biotin. (B) Incubation of streptavidin (STV), BSA, and fluorescent biotin. Diagram of the patterned areas on the substrate. (C) Plot of normalized fluorescence intensity values for three test areas with fluorescent microscopy images.

During imaging, the boundaries of the patterned areas were distinct under the microscope, which suggested successful results. The areas passivated with BSA are darker than the areas with biotin applied. However, the fluorescence intensity was brighter in the areas with biotin on APTES than biotin on streptavidin (Fig. 4.3c). This is contrary to the expected results. The fluorescence signal was expected to be higher in the area with biotin on streptavidin compared to any of the other areas. The biotin likely attached to the APTES non-specifically, creating a high fluorescence signal in that area. This makes it difficult to validate the appropriate functionalization steps. Additionally, the electrostatic binding between the streptavidin to the APTES is unpredictable.

Improving these functionalization issues is vital for proper surface functionalization and the validation of each step. Future work for the functionalization is discussed in Chapter Five.

CHAPTER FIVE

Conclusions and Future Work

Conclusions

In this work, the goal was to address a common issue in cell adhesion studies and non-specific adsorption in biosensing: the inability to generate a high shear stress in a microchannel. A hydrodynamic method of non-specific binding or cell detachment utilizing a trapezoidal microchannel was investigated. The narrower channel height at the ROI creates and area of high shear stress, while the rest of the channel maintains a lower shear stress. The fluid dynamics were compared to a straight microchannel with the same height at the ROI (50 μm). The results demonstrate the trapezoidal microchannels can produce a wall shear stress 99.5% of the wall shear stress in the straight microchannel (4.96 Pa vs. 4.98 Pa), with 13% and 29% of the pressure drop (259 Pa and 589 Pa vs. 1999 Pa), where two different trapezoidal lengths were analyzed, L_g = 0.5 and 2.5 mm respectively. Additionally, the trapezoidal microchannels can hold 90 or 80 times the volume of the straight channel (21.8 μL and 19.8 μL vs. 0.25 μL). These results promote the possibility of using this microfluidic design for generating a high critical wall shear stress for cell or biomolecule detachment, while maintaining a lower pressure drop and holding a larger fluid capacity. This design also has the benefit of flexibility outside of the ROI for easy integration of other microfluidic components. Also in this work, the limitation of reproducibility in fabricating biosensors was examined by 3D printing

trapezoidal microchannels. Preliminary surface functionalization protocol was established for the immobilization of bioreceptors for experimental validation of this work.

Future Work

Fluid Dynamics Evaluation

Additional optimization of the trapezoidal microchannel could be done to further minimize the pressure loss. In these simulations, only a limited number of cases were run for $\boldsymbol{\ell}$ and L_T. Also, $\boldsymbol{\ell^*}$ could be optimized since in these simulations $\boldsymbol{\ell}$ was kept equal to $\boldsymbol{\ell^*}$. The exact channel geometry would need to be specified for a particular application. A way to relate the trapezoidal channel geometry based on the desired shear stress and pressure drop would be beneficial.

3D Printing

Further optimization of the resin printing would be beneficial. Different geometries would enhance the evaluation of print capability. The feature measurements were made using microscopy. Validation of the additional measurements, especially for the elevation of the trapezoidal structures, would be beneficial.

Functionalization

The results suggest a more reliable method of attaching the streptavidin to the APTES surface is needed, such as using Sulfo-NHS-biotin. Validation other than through fluorescence microscopy could be useful, such as the attachment of microspheres, or using UV-Vis spectroscopy. After successful demonstration of the protocol on the glass substrate, the protocol should be demonstrated on the resin substrate. While surface

functionalization has been demonstrated on a 3D printed resin, it has not been applied to the B9 resins, to the author's knowledge.

APPENDICES

APPENDIX A

Supporting Fluid Dynamics Calculations

To determine the inlet velocity needed to achieve τ_c = 5 Pa in microchannel in Channel A (h = 50 μm), the wall shear stress equation is used with the parameters defined in Chapter Three:

$$\tau_w = \frac{6\eta U}{h}$$

$$5\ \text{Pa} = \frac{6(0.00089\ \text{Pa}\cdot\text{s})U}{(50\times10^{-6}\ \text{m})}$$

$$U_A = 4.68\ \times 10^{-2}\,\frac{\text{m}}{\text{s}}$$

Use the same flow rate to calculate the velocity for channel B (h = 500 μm). Since in 2D, use Q/w:

$$\frac{Q_A}{w_A} = \frac{Q_B}{w_B}$$

$$U_A h_A = U_B h_B$$

$$(4.68\times10^{-2}\,\frac{\text{m}}{\text{s}})(50\times10^{-6}\ \text{m}) = U_B(500\times10^{-6}\ \text{m})$$

$$U_B = 4.68\times10^{-3}\,\frac{\text{m}}{\text{s}}$$

Calculate the pressure drop:

$$\Delta P = -\frac{12\eta Q L}{w h^3}$$

For Channel A: h = 50 μm

$$\Delta P = \frac{12(8.9 \times 10^{-4}\ \text{Pa} \cdot \text{s})\left(4.68\ \times 10^{-2}\ \frac{\text{m}}{\text{s}}\right)(0.01\ \text{m})}{(50\ \times 10^{-6}\ \text{m})^2}$$

$$\Delta P = 2000\ \text{Pa}$$

For Channel B: h = 500 μm

$$\Delta P = \frac{12(8.9\ \times 10^{-4}\ \text{Pa} \cdot \text{s})\left(4.68\ \times 10^{-3}\ \frac{\text{m}}{\text{s}}\right)(0.01\ \text{m})}{(500 \times 10^{-6}\ \text{m})^2},$$

$$\Delta P = 2\ \text{Pa}$$

Calculate Reynolds Number:

$$Re = \frac{\rho \bar{U} h}{\eta}$$

For Channel A: h = 50 μm

$$Re = \frac{(997\ \frac{\text{kg}}{\text{m}^3})(4.68\ \times 10^{-2}\ \frac{\text{m}}{\text{s}})(50 \times 10^{-6}\ \text{m})}{8.9\ \times 10^{-4}\ \text{Pa} \cdot \text{s}}$$

$$Re = 2.62$$

For Channel B: h = 500 μm

$$Re = \frac{(997\ \frac{\text{kg}}{\text{m}^3})(4.68\ \times 10^{-3}\ \frac{\text{m}}{\text{s}})(500 \times 10^{-6}\ \text{m})}{8.9\ \times 10^{-4}\ \text{Pa} \cdot \text{s}}$$

$$Re = 2.62$$

Calculate Entrance length:

$$L_e\ \approx 0.05(Re)(h)$$

For Channel A: h = 50 μm

$$L_e \approx 0.05(2.62)(50\ \mu\text{m})$$

$$L_e \approx 65.5\ \mu\text{m}$$

For Channel B: h = 500 μm

$$L_e \approx 0.05(2.62)(500\ \mu\text{m})$$

$$L_e \approx 655\ \mu\text{m}$$

APPENDIX B

CFD Simulation File Example

Below is an example .gfs code used for trapezoidal microchannel E with comments to the right of the arrows.

```
20 19 GfsSimulation GfsBox GfsGEdge {} {
  Global {
        #define width 500.e-6                          → channel height
        #define rho_f 997.0                            → fluid density
        #define mu_f  8.9e-4                           → fluid viscosity

        #define LevelMax 8                             → mesh refinement levels
        #define LevelMin 3

        #define Uin 0.0046816479                       → inlet velocity
  }
  Time { end = 4 dtmax = 1e-4 }
  Refine 6

  Solid ( x < 4.5e-3 ? y - (225e-6*tanh((x-3.9e-3)/200e-6)-25e-6): x >= 4.5e-3 && x <
5.e-3 ? y - 200.e-6 : y-(225e-6*tanh((5.6e-3-x)/200e-6)-25e-6) )
  RefineSolid 8                                        → trapezoidal structure defined

  SourceViscosity mu_f

  PhysicalParams {
        L     = width
        alpha = 1./rho_f
  }

  AdaptGradient { istep = 5 } { minlevel = LevelMin maxlevel = (x>3.8e-3 && x <
5.7e-3 ? LevelMax:LevelMax-2) cmax = 1e-4} U

  # Dynamic load-balancing
  EventBalance { istep = 5 } 0.1

  OutputTime { istep = 5 } time.dat
  OutputBalance { istep = 5 } balance.dat

  # Save a (single) snapshot every 100 timesteps
```

```
   OutputSimulation { istep = 100 } snapshot-%ld.vtk { format=VTK }
   GfsEventStop {istep = 1} U 1e-10 DU
   OutputSimulation { start = end } final_snapshot-%ld.vtk { format =VTK }
   OutputLocation {start = end} data0 4.75e-3 200.e-6 0.0
   OutputLocation {start = end} data1 4.75e-3 202.e-6 0.0
   OutputLocation {start = end} data2 4.75e-3 204.e-6 0.0
}
GfsBox {
   top = Boundary {
            BcDirichlet U 0
            BcDirichlet V 0
   }
   bottom = Boundary {
            BcDirichlet U 0
            BcDirichlet V 0
   }
   left = Boundary {
            BcDirichlet U Uin
   }
}
GfsBox {
   top = Boundary {
            BcDirichlet U 0
            BcDirichlet V 0
   }
   bottom = Boundary {
            BcDirichlet U 0
            BcDirichlet V 0
   }
}
.
.          → A total of 20 boxes are defined (L = 20*500 μm = 1 cm), only 3 shown
.
GfsBox {
   top = Boundary {
            BcDirichlet U 0
            BcDirichlet V 0
   }
   bottom = Boundary {
            BcDirichlet U 0
            BcDirichlet V 0
   }
   right = BoundaryOutflow
}
1 2 right                    → sequential order of boxes that make up channel length
2 3 right
```

3 4 right
4 5 right
5 6 right
6 7 right
7 8 right
8 9 right
9 10 right
10 11 right
11 12 right
12 13 right
13 14 right
14 15 right
15 16 right
16 17 right
17 18 right
18 19 right
19 20 right

REFERENCES

[1] A. Ahmad Khalili and M. R. Ahmad, "A Review of Cell Adhesion Studies for Biomedical and Biological Applications," *Int. J. Mol. Sci.*, vol. 16, no. 8, pp. 18149–18184, Aug. 2015.

[2] S. Chen and M. H. Shamsi, "Biosensors-on-chip: a topical review," *J. Micromechanics Microengineering*, vol. 27, no. 8, p. 083001, 2017.

[3] S. Choi and J. Chae, "Methods of reducing non-specific adsorption in microfluidic biosensors," *J. Micromechanics Microengineering*, vol. 20, no. 7, p. 075015, 2010.

[4] A. Carré and K. L. Mittal, *Surface and Interfacial Aspects of Cell Adhesion*. CRC Press, 2011.

[5] S. Kou *et al.*, "A multishear microfluidic device for quantitative analysis of calcium dynamics in osteoblasts," *Biochem. Biophys. Res. Commun.*, vol. 408, no. 2, pp. 350–355, May 2011.

[6] D. Huber, A. Oskooei, X. Casadevall i Solvas, A. deMello, and G. V. Kaigala, "Hydrodynamics in Cell Studies," *Chem. Rev.*, vol. 118, no. 4, pp. 2042–2079, Feb. 2018.

[7] M. M. Gong and D. Sinton, "Turning the Page: Advancing Paper-Based Microfluidics for Broad Diagnostic Application," *Chem. Rev.*, vol. 117, no. 12, pp. 8447–8480, Jun. 2017.

[8] K. Yamada, H. Shibata, K. Suzuki, and D. Citterio, "Toward practical application of paper-based microfluidics for medical diagnostics: state-of-the-art and challenges," *Lab. Chip*, vol. 17, no. 7, pp. 1206–1249, Mar. 2017.

[9] N. J. Ronkainen, H. B. Halsall, and W. R. Heineman, "Electrochemical biosensors," *Chem. Soc. Rev.*, vol. 39, no. 5, pp. 1747–1763, Apr. 2010.

[10] J. Brake, "Design and Experimental Demonstration of a Low-cost, Multiplexable Optical Cavity Based Biosensor for Point of Care Diagnosis," LeTourneau University, Longview, Texas, 2014.

[11] "FISITECH | The Way of Never Give Up: Introduction to Biosensor," *FISITECH | The Way of Never Give Up*, 15-Aug-2011. .

[12] E. Reimhult and F. Höök, “Design of Surface Modifications for Nanoscale Sensor Applications,” *Sensors*, vol. 15, no. 1, pp. 1635–1675, Jan. 2015.

[13] G. Wang, R. Han, X. Su, Y. Li, G. Xu, and X. Luo, “Zwitterionic peptide anchored to conducting polymer PEDOT for the development of antifouling and ultrasensitive electrochemical DNA sensor,” *Biosens. Bioelectron.*, vol. 92, pp. 396–401, Jun. 2017.

[14] H. A. Alhadrami, “Biosensors: Classifications, medical applications, and future prospective,” *Biotechnol. Appl. Biochem.*, vol. 65, no. 3, pp. 497–508, 2018.

[15] S. Choi, M. Goryll, L. Y. M. Sin, P. K. Wong, and J. Chae, “Microfluidic-based biosensors toward point-of-care detection of nucleic acids and proteins,” *Microfluid. Nanofluidics*, vol. 10, no. 2, pp. 231–247, Feb. 2011.

[16] L. Soleymani and F. Li, “Mechanistic Challenges and Advantages of Biosensor Miniaturization into the Nanoscale,” *ACS Sens.*, vol. 2, no. 4, pp. 458–467, Apr. 2017.

[17] D. G. Rackus, M. H. Shamsi, and A. R. Wheeler, “Electrochemistry, biosensors and microfluidics: a convergence of fields,” *Chem. Soc. Rev.*, vol. 44, no. 15, pp. 5320–5340, 2015.

[18] G. Luka *et al.*, “Microfluidics Integrated Biosensors: A Leading Technology towards Lab-on-a-Chip and Sensing Applications,” *Sensors*, vol. 15, no. 12, pp. 30011–30031, Dec. 2015.

[19] S. Prakash, M. Pinti, and B. Bhushan, “Theory, fabrication and applications of microfluidic and nanofluidic biosensors,” *Philos. Trans. Math. Phys. Eng. Sci.*, vol. 370, no. 1967, pp. 2269–2303, 2012.

[20] C. Rivet, H. Lee, A. Hirsch, S. Hamilton, and H. Lu, “Microfluidics for medical diagnostics and biosensors,” *Chem. Eng. Sci.*, vol. 66, no. 7, pp. 1490–1507, Apr. 2011.

[21] F. S. Felix and L. Angnes, “Electrochemical immunosensors – A powerful tool for analytical applications,” *Biosens. Bioelectron.*, vol. 102, pp. 470–478, Apr. 2018.

[22] J. Min *et al.*, “Integrated Biosensor for Rapid and Point-of-Care Sepsis Diagnosis,” *ACS Nano*, Mar. 2018.

[23] A. Ramanavičius, A. Ramanavičienė, and A. Malinauskas, “Electrochemical sensors based on conducting polymer—polypyrrole,” *Electrochimica Acta*, vol. 51, no. 27, pp. 6025–6037, Aug. 2006.

[24] M. L. Sin, K. E. Mach, P. K. Wong, and J. C. Liao, “Advances and challenges in biosensor-based diagnosis of infectious diseases,” *Expert Rev. Mol. Diagn.*, vol. 14, no. 2, pp. 225–244, Mar. 2014.

[25] Michelle H. Grandin and Marcus Textor, Eds., *Intelligent Surfaces in Biotechnology: Scientific and Engineering Concepts, Enabling Technologies, and Translation to Bio-Oriented Applications*. 2012.

[26] R. Singh, S. K. R. S. Sankaranarayanan, and V. R. Bhethanabotla, “Orthogonal surface acoustic wave device based on langasite for simultaneous biosensing and biofouling removal,” *Appl. Phys. Lett.*, vol. 94, no. 26, p. 263503, Jun. 2009.

[27] A. Ahluwalia, G. Giusto, and D. De Rossi, “Non-specific adsorption on antibody surfaces for immunosensing,” *Mater. Sci. Eng. C*, vol. 3, no. 3, pp. 267–271, Dec. 1995.

[28] J. E. Contreras-Naranjo and O. Aguilar, “Suppressing Non-Specific Binding of Proteins onto Electrode Surfaces in the Development of Electrochemical Immunosensors,” *Biosensors*, vol. 9, no. 1, p. 15, Mar. 2019.

[29] H. Ogi, Y. Fukunishi, H. Nagai, K. Okamoto, M. Hirao, and M. Nishiyama, “Nonspecific-adsorption behavior of polyethylenglycol and bovine serum albumin studied by 55-MHz wireless–electrodeless quartz crystal microbalance,” *Biosens. Bioelectron.*, vol. 24, no. 10, pp. 3148–3152, Jun. 2009.

[30] V. Ettelt, K. Ekat, P. W. Kämmerer, B. Kreikemeyer, M. Epple, and M. Veith, “Streptavidin-coated surfaces suppress bacterial colonization by inhibiting non-specific protein adsorption,” *J. Biomed. Mater. Res. A*, vol. 106, no. 3, pp. 758–768, 2018.

[31] J. G. Kenna, G. N. Major, and R. S. Williams, “Methods for reducing non-specific antibody binding in enzyme-linked immunosorbent assays,” *J. Immunol. Methods*, vol. 85, no. 2, pp. 409–419, Dec. 1985.

[32] Salta Maria *et al.*, “Designing biomimetic antifouling surfaces,” *Philos. Trans. R. Soc. Math. Phys. Eng. Sci.*, vol. 368, no. 1929, pp. 4729–4754, Oct. 2010.

[33] D. V. Manov, G. C. Chang, and T. D. Dickey, “Methods for Reducing Biofouling of Moored Optical Sensors,” *J. Atmospheric Ocean. Technol.*, vol. 21, no. 6, pp. 958–968, Jun. 2004.

[34] B. D. Ratner, A. S. Hoffman, F. J. Schoen, and J. E. Lemons, *Biomaterials Science: An Introduction to Materials in Medicine*. Academic Press, 2012.

[35] S. Pan, H. Zhang, W. Liu, Y. Wang, W. Pang, and X. Duan, “Biofouling Removal and Protein Detection Using a Hypersonic Resonator,” *ACS Sens.*, vol. 2, no. 8, pp. 1175–1183, Aug. 2017.

[36] R. Vaidyanathan, L. M. van Leeuwen, S. Rauf, M. J. A. Shiddiky, and M. Trau, “A Multiplexed Device Based on Tunable *Nanoshearing* for Specific Detection of Multiple Protein Biomarkers in Serum,” *Sci. Rep.*, vol. 5, p. 9756, May 2015.

[37] “Glossary | Publications and Other Information | BTSC.” [Online]. Available: https://brownfieldstsc.org/glossary.cfm?q=1. [Accessed: 09-Dec-2018].

[38] Y. Zhang, V. Lyons, and D. Pappas, “Fundamentals of affinity cell separations,” *ELECTROPHORESIS*, p. n/a-n/a, 2018.

[39] F. Brandtzaeg, “Conjugates of Immunoglobulin G with Different Fluorochromes,” *Scand. J. Immunol.*, vol. 2, no. 4, pp. 333–348, 1973.

[40] B. Liu *et al.*, “Design and mechanisms of antifouling materials for surface plasmon resonance sensors,” *Acta Biomater.*, vol. 40, pp. 100–118, Aug. 2016.

[41] C. E. Soteropulos, K. M. Zurick, M. T. Bernards, and H. K. Hunt, “Tailoring the Protein Adsorption Properties of Whispering Gallery Mode Optical Biosensors,” *Langmuir*, vol. 28, no. 44, pp. 15743–15750, Nov. 2012.

[42] J. Schartner *et al.*, “Universal Method for Protein Immobilization on Chemically Functionalized Germanium Investigated by ATR-FTIR Difference Spectroscopy,” *J. Am. Chem. Soc.*, vol. 135, no. 10, pp. 4079–4087, Mar. 2013.

[43] P. Tengvall, I. Lundström, and B. Liedberg, “Protein adsorption studies on model organic surfaces: an ellipsometric and infrared spectroscopic approach,” *Biomaterials*, vol. 19, no. 4, pp. 407–422, Mar. 1998.

[44] K. Hinrichs *et al.*, “Analysis of biosensors by chemically specific optical techniques. Chemiluminescence-imaging and infrared spectroscopic mapping ellipsometry,” *Anal. Bioanal. Chem.*, vol. 387, no. 5, pp. 1823–1829, Mar. 2007.

[45] J. B. Schlenoff, “Zwitteration: Coating Surfaces with Zwitterionic Functionality to Reduce Nonspecific Adsorption,” *Langmuir*, vol. 30, no. 32, pp. 9625–9636, Aug. 2014.

[46] H. Zhang and M. Chiao, “Anti-fouling Coatings of Poly(dimethylsiloxane) Devices for Biological and Biomedical Applications,” *J. Med. Biol. Eng.*, vol. 35, no. 2, pp. 143–155, Apr. 2015.

[47] S. Sheikh, C. Blaszykowski, and M. Thompson, “Sacrificial BSA to block non-specific adsorption on organosilane adlayers in ultra-high frequency acoustic wave sensing,” *Surf. Interface Anal.*, vol. 45, no. 11–12, pp. 1781–1784, Nov. 2013.

[48] M. V. Riquelme, H. Zhao, V. Srinivasaraghavan, A. Pruden, P. Vikesland, and M. Agah, “Optimizing blocking of nonspecific bacterial attachment to impedimetric biosensors,” *Sens. Bio-Sens. Res.*, vol. 8, pp. 47–54, May 2016.

[49] D. E. Tacha and L. McKinney, “Casein Reduces Nonspecific Background Staining in Immunolabeling Techniques,” *J. Histotechnol.*, vol. 15, no. 2, pp. 127–132, Jun. 1992.

[50] M. Steinitz, “Quantitation of the Blocking Effect of Tween 20 and Bovine Serum Albumin in ELISA Microwells,” *Anal. Biochem.*, vol. 282, no. 2, pp. 232–238, Jul. 2000.

[51] X. Muñoz-Berbel, N. Godino, O. Laczka, E. Baldrich, F. X. Muñoz, and F. J. del Campo, “Impedance-Based Biosensors for Pathogen Detection,” in *Principles of Bacterial Detection: Biosensors, Recognition Receptors and Microsystems*, M. Zourob, S. Elwary, and A. Turner, Eds. New York, NY: Springer New York, 2008, pp. 341–376.

[52] “Practical Tips of ELISA,” *Creative Diagnostics*. [Online]. Available: https://www.creative-diagnostics.com/Practical-Tips-of-ELISA.htm. [Accessed: 09-Dec-2018].

[53] B. N. Johnson and R. Mutharasan, “Reduction of nonspecific protein adsorption on cantilever biosensors caused by transverse resonant mode vibration,” *Analyst*, vol. 139, no. 5, pp. 1112–1120, 2014.

[54] F. Palmisano, C. Malitesta, D. Centonze, and P. G. Zambonin, “Correlation between Permselectivity and Chemical Structure of Overoxidized Polypyrrole Membranes Used in Electroproduced Enzyme Biosensors,” *Anal. Chem.*, vol. 67, no. 13, pp. 2207–2211, Jul. 1995.

[55] Y. Lin, F. Lu, Y. Tu, and Z. Ren, “Glucose Biosensors Based on Carbon Nanotube Nanoelectrode Ensembles,” *Nano Lett.*, vol. 4, no. 2, pp. 191–195, Feb. 2004.

[56] X. Chen, N. Matsumoto, Y. Hu, and G. S. Wilson, “Electrochemically Mediated Electrodeposition/Electropolymerization To Yield a Glucose Microbiosensor with Improved Characteristics,” *Anal. Chem.*, vol. 74, no. 2, pp. 368–372, Jan. 2002.

[57] A. P. Soldatkin *et al.*, “Glucose sensitive conductometric biosensor with additional Nafion membrane: reduction of influence of buffer capacity on the sensor response and extension of its dynamic range,” *Anal. Chim. Acta*, vol. 288, no. 3, pp. 197–203, Apr. 1994.

[58] S.-Y. Jung *et al.*, “The Vroman Effect: A Molecular Level Description of Fibrinogen Displacement,” *J. Am. Chem. Soc.*, vol. 125, no. 42, pp. 12782–12786, Oct. 2003.

[59] L. Vroman and A. L. Adams, “Findings with the recording ellipsometer suggesting rapid exchange of specific plasma proteins at liquid/solid interfaces,” *Surf. Sci.*, vol. 16, pp. 438–446, Aug. 1969.

[60] “Application Note: 110 - Studying Protein Adsorption Properties with SPR,” *Biosensing Instrument*. .

[61] S. Choi and J. Chae, “Surface plasmon resonance biosensor based on Vroman effect : Towards cancer biomarker detection,” in *2009 IEEE 15th International Mixed-Signals, Sensors, and Systems Test Workshop*, 2009, pp. 1–3.

[62] P. Charles *et al.*, “Reduction of Non-Specific Protein Adsorption Using Poly(ethylene) Glycol (PEG) Modified Polyacrylate Hydrogels In Immunoassays for Staphylococcal Enterotoxin B Detection,” *Sensors*, vol. 9, no. 1, pp. 645–655, Jan. 2009.

[63] “Poly(ethylene glycol) Monolayer Formation and Stability on Gold and Silicon Nitride Substrates - Langmuir (ACS Publications).” [Online]. Available: https://pubs.acs.org/doi/abs/10.1021/la801357v. [Accessed: 08-Apr-2019].

[64] T. Wink, S. J. van Zuilen, A. Bult, and W. P. van Bennekom, “Self-assembled Monolayers for Biosensors,” *Analyst*, vol. 122, no. 4, pp. 43R-50R, 1997.

[65] R. Dahint, R. Ros Seigel, P. Harder, M. Grunze, and F. Josse, “Detection of non-specific protein adsorption at artificial surfaces by the use of acoustic plate mode sensors,” *Sens. Actuators B Chem.*, vol. 36, no. 1–3, pp. 497–505, Oct. 1996.

[66] G. Zuo *et al.*, “Dual-SAM functionalization on integrated cantilevers for specific trace-explosive sensing and non-specific adsorption suppression,” *Nanotechnology*, vol. 18, no. 25, p. 255501, 2007.

[67] O. R. Bolduc and J.-F. Masson, “Monolayers of 3-Mercaptopropyl-amino Acid to Reduce the Nonspecific Adsorption of Serum Proteins on the Surface of Biosensors,” *Langmuir*, vol. 24, no. 20, pp. 12085–12091, Oct. 2008.

[68] J. Ladd, Z. Zhang, S. Chen, J. C. Hower, and S. Jiang, “Zwitterionic Polymers Exhibiting High Resistance to Nonspecific Protein Adsorption from Human Serum and Plasma,” *Biomacromolecules*, vol. 9, no. 5, pp. 1357–1361, May 2008.

[69] E. van Andel *et al.*, “Systematic Comparison of Zwitterionic and Non-Zwitterionic Antifouling Polymer Brushes on a Bead-Based Platform,” *Langmuir*, vol. 35, no. 5, pp. 1181–1191, Feb. 2019.

[70] A. Laschewsky, “Structures and Synthesis of Zwitterionic Polymers,” *Polymers*, vol. 6, no. 5, pp. 1544–1601, May 2014.

[71] S. K. R. S. Sankaranarayanan, S. Cular, V. R. Bhethanabotla, and B. Joseph, “Flow induced by acoustic streaming on surface-acoustic-wave devices and its application in biofouling removal: A computational study and comparisons to experiment,” *Phys. Rev. E*, vol. 77, no. 6, p. 066308, Jun. 2008.

[72] R. Gref *et al.*, “‘Stealth’ corona-core nanoparticles surface modified by polyethylene glycol (PEG): influences of the corona (PEG chain length and surface density) and of the core composition on phagocytic uptake and plasma protein adsorption,” *Colloids Surf. B Biointerfaces*, vol. 18, no. 3, pp. 301–313, Oct. 2000.

[73] K. L. Prime and G. M. Whitesides, “Adsorption of proteins onto surfaces containing end-attached oligo(ethylene oxide): a model system using self-assembled monolayers,” 1993.

[74] P.-Y. J. Yeh, J. N. Kizhakkedathu, J. D. Madden, and Mu. Chiao, “Electric field and vibration-assisted nanomolecule desorption and anti-biofouling for biosensor applications,” *Colloids Surf. B Biointerfaces*, vol. 59, no. 1, pp. 67–73, Sep. 2007.

[75] P. H. Dykstra, V. Roy, C. Byrd, W. E. Bentley, and R. Ghodssi, “Microfluidic Electrochemical Sensor Array for Characterizing Protein Interactions with Various Functionalized Surfaces,” *Anal. Chem.*, vol. 83, no. 15, pp. 5920–5927, Aug. 2011.

[76] K. M. Ainslie, G. Sharma, M. A. Dyer, C. A. Grimes, and M. V. Pishko, “Attenuation of Protein Adsorption on Static and Oscillating Magnetostrictive Nanowires,” *Nano Lett.*, vol. 5, no. 9, pp. 1852–1856, Sep. 2005.

[77] M. Bernards and Y. He, “Polyampholyte polymers as a versatile zwitterionic biomaterial platform,” *J. Biomater. Sci. Polym. Ed.*, vol. 25, no. 14–15, pp. 1479–1488, Oct. 2014.

[78] L. S. Roach, H. Song, and R. F. Ismagilov, “Controlling Nonspecific Protein Adsorption in a Plug-Based Microfluidic System by Controlling Interfacial Chemistry Using Fluorous-Phase Surfactants,” *Anal. Chem.*, vol. 77, no. 3, pp. 785–796, Feb. 2005.

[79] H. Shi, W.-B. Tsai, M. D. Garrison, S. Ferrari, and B. D. Ratner, “Template-imprinted nanostructured surfaces for protein recognition,” *Nature*, vol. 398, no. 6728, p. 593, Apr. 1999.

[80] G. Guan, B. Liu, Z. Wang, and Z. Zhang, “Imprinting of Molecular Recognition Sites on Nanostructures and Its Applications in Chemosensors,” *Sensors*, vol. 8, no. 12, pp. 8291–8320, Dec. 2008.

[81] C.-K. Lee, Y.-M. Wang, L.-S. Huang, and S. Lin, “Atomic force microscopy: Determination of unbinding force, off rate and energy barrier for protein–ligand interaction,” *Micron*, vol. 38, no. 5, pp. 446–461, Jul. 2007.

[82] M. J. A. Shiddiky, R. Vaidyanathan, S. Rauf, Z. Tay, and M. Trau, “Molecular *Nanoshearing*: An Innovative Approach to Shear off Molecules with AC-Induced Nanoscopic Fluid Flow,” *Sci. Rep.*, vol. 4, p. 3716, Jan. 2014.

[83] R. Vaidyanathan *et al.*, “Detecting Exosomes Specifically: A Multiplexed Device Based on Alternating Current Electrohydrodynamic Induced Nanoshearing,” *Anal. Chem.*, vol. 86, no. 22, pp. 11125–11132, Nov. 2014.

[84] R. Vaidyanathan, M. J. A. Shiddiky, S. Rauf, E. Dray, Z. Tay, and M. Trau, “Tunable ‘Nano-Shearing’: A Physical Mechanism to Displace Nonspecific Cell Adhesion During Rare Cell Detection,” *Anal. Chem.*, vol. 86, no. 4, pp. 2042–2049, Feb. 2014.

[85] Y. Wang, R. Vaidyanathan, M. J. A. Shiddiky, and M. Trau, “Enabling Rapid and Specific Surface-Enhanced Raman Scattering Immunoassay Using Nanoscaled Surface Shear Forces,” *ACS Nano*, vol. 9, no. 6, pp. 6354–6362, Jun. 2015.

[86] R. Vaidyanathan, S. Dey, L. G. Carrascosa, M. J. A. Shiddiky, and M. Trau, “Alternating current electrohydrodynamics in microsystems: Pushing biomolecules and cells around on surfaces,” *Biomicrofluidics*, vol. 9, no. 6, p. 061501, Nov. 2015.

[87] S. K. R. S. Sankaranarayanan, R. Singh, and V. R. Bhethanabotla, “Acoustic streaming induced elimination of nonspecifically bound proteins from a surface acoustic wave biosensor: Mechanism prediction using fluid-structure interaction models,” *J. Appl. Phys.*, vol. 108, no. 10, p. 104507, Nov. 2010.

[88] S. Cular, D. W. Branch, V. R. Bhethanabotla, G. D. Meyer, and H. G. Craighead, “Removal of Nonspecifically Bound Proteins on Microarrays Using Surface Acoustic Waves,” *IEEE Sens. J.*, vol. 8, no. 3, pp. 314–320, Mar. 2008.

[89] M. B. Richardson and V. R. Bhethanabotla, “Orthogonal SAW transducers on substrate for simultaneous biofouling removal and biosensing,” 10031140, 24-Jul-2018.

[90] W.-T. Hsu, G.-H. Feng, C.-L. Cho, and L.-K. Chau, “Nonspecific binding removal and specific binding regeneration using longitudinal acoustic waves,” *RSC Adv.*, vol. 3, no. 36, pp. 16159–16166, 2013.

[91] X. Duan, S. Pan, and W. Pang, “Development of high-frequency bulk acoustic wave (BAW) resonators as biosensors and bioactuators,” in *2017 IEEE International Electron Devices Meeting (IEDM)*, 2017, pp. 10.2.1-10.2.4.

[92] M. Zhang *et al.*, “Kinetic studies of microfabricated biosensors using local adsorption strategy,” *Biosens. Bioelectron.*, vol. 74, pp. 8–15, Dec. 2015.

[93] D. Li, C. Wang, G. Sun, S. Senapati, and H.-C. Chang, “A shear-enhanced CNT-assembly nanosensor platform for ultra-sensitive and selective protein detection,” *Biosens. Bioelectron.*, vol. 97, pp. 143–149, Nov. 2017.

[94] B. N. Johnson and R. Mutharasan, “Biosensing using dynamic-mode cantilever sensors: A review,” *Biosens. Bioelectron.*, vol. 32, no. 1, pp. 1–18, Feb. 2012.

[95] I. Dufour *et al.*, “Effect of hydrodynamic force on microcantilever vibrations: Applications to liquid-phase chemical sensing,” *Sens. Actuators B Chem.*, vol. 192, pp. 664–672, Mar. 2014.

[96] K. M. Goeders, J. S. Colton, and L. A. Bottomley, “Microcantilevers: Sensing Chemical Interactions via Mechanical Motion,” *Chem. Rev.*, vol. 108, no. 2, pp. 522–542, Feb. 2008.

[97] Q. Zhu, “Microcantilever Sensors in Biological and Chemical Detections,” *Sens. Transducers Tor.*, vol. 125, no. 2, pp. 1–21, Feb. 2011.

[98] A. Boisen, S. Dohn, S. S. Keller, S. Schmid, and M. Tenje, “Cantilever-like micromechanical sensors,” *Rep. Prog. Phys.*, vol. 74, no. 3, p. 036101, Feb. 2011.

[99] X. Li and D.-W. Lee, “Integrated microcantilevers for high-resolution sensing and probing,” *Meas. Sci. Technol.*, vol. 23, no. 2, p. 022001, Dec. 2011.

[100] A. P. Haring, E. Cesewski, and B. N. Johnson, “Piezoelectric Cantilever Biosensors for Label-free, Real-time Detection of DNA and RNA,” in *Biosensors and Biodetection: Methods and Protocols, Volume 2: Electrochemical, Bioelectronic, Piezoelectric, Cellular and Molecular Biosensors*, B. Prickril and A. Rasooly, Eds. New York, NY: Springer New York, 2017, pp. 247–262.

[101] G. J. Brereton and Q. Qi, “Mechanisms of removal of micron-sized particles by high-frequency ultrasonic waves,” *IEEE Trans. Ultrason. Ferroelectr. Freq. Control*, vol. 42, no. 4, pp. 619–629, Jul. 1995.

[102] J. Lei, P. Glynne-Jones, and M. Hill, “Acoustic streaming in the transducer plane in ultrasonic particle manipulation devices,” *Lab. Chip*, vol. 13, no. 11, pp. 2133–2143, 2013.

[103] R. M. Lec and P. A. Lewin, “Acoustic wave biosensors,” in *Proceedings of the 20th Annual International Conference of the IEEE Engineering in Medicine and Biology Society. Vol.20 Biomedical Engineering Towards the Year 2000 and Beyond (Cat. No.98CH36286)*, 1998, vol. 6, pp. 2779–2784 vol.6.

[104] K. Länge, B. E. Rapp, and M. Rapp, “Surface acoustic wave biosensors: a review,” *Anal. Bioanal. Chem.*, vol. 391, no. 5, pp. 1509–1519, Jul. 2008.

[105] R. Fogel, J. Limson, and A. A. Seshia, “Acoustic biosensors,” *Essays Biochem.*, vol. 60, no. 1, pp. 101–110, Jun. 2016.

[106] L. Y. Yeo and J. R. Friend, “Surface Acoustic Wave Microfluidics,” *Annu. Rev. Fluid Mech.*, vol. 46, no. 1, pp. 379–406, 2014.

[107] J. Friend and L. Y. Yeo, “Microscale acoustofluidics: Microfluidics driven via acoustics and ultrasonics,” *Rev. Mod. Phys.*, vol. 83, no. 2, pp. 647–704, Jun. 2011.

[108] H. Bruus *et al.*, “Forthcoming Lab on a Chip tutorial series on acoustofluidics: Acoustofluidics—exploiting ultrasonic standing wave forces and acoustic streaming in microfluidic systems for cell and particle manipulation,” *Lab. Chip*, vol. 11, no. 21, pp. 3579–3580, Oct. 2011.

[109] P. Jönsson, A. Gunnarsson, and F. Höök, “Accumulation and Separation of Membrane-Bound Proteins Using Hydrodynamic Forces,” *Anal. Chem.*, vol. 83, no. 2, pp. 604–611, Jan. 2011.

[110] G. M. Burdick, N. S. Berman, and S. P. Beaudoin, “Hydrodynamic particle removal from surfaces,” *Thin Solid Films*, vol. 488, no. 1, pp. 116–123, Sep. 2005.

[111] G. M. Burdick, N.S. Berman, and S.P. Beaudoin, “Describing Hydrodynamic Particle Removal from Surfaces Using the Particle Reynolds Number,” *J. Nanoparticle Res.*, vol. 3, no. 5–6, pp. 453–465, 2001.

[112] M. S. Munson, M. S. Hasenbank, E. Fu, and P. Yager, “Suppression of non-specific adsorption using sheath flow,” *Lab. Chip*, vol. 4, no. 5, pp. 438–445, Oct. 2004.

[113] K. R. Hawkins, M. R. Steedman, R. R. Baldwin, E. Fu, S. Ghosal, and P. Yager, “A method for characterizing adsorption of flowing solutes to microfluidic device surfaces,” *Lab. Chip*, vol. 7, no. 2, pp. 281–285, 2007.

[114] G. M. Walker, H. C. Zeringue, and D. J. Beebe, “Microenvironment design considerations for cellular scale studies,” *Lab. Chip*, vol. 4, no. 2, pp. 91–97, 2004.

[115] C. Couzon, A. Duperray, and C. Verdier, “Critical stresses for cancer cell detachment in microchannels,” *Eur. Biophys. J.*, vol. 38, no. 8, pp. 1035–1047, Oct. 2009.

[116] H. Lu, L. Y. Koo, W. M. Wang, D. A. Lauffenburger, L. G. Griffith, and K. F. Jensen, “Microfluidic Shear Devices for Quantitative Analysis of Cell Adhesion,” *Anal. Chem.*, vol. 76, no. 18, pp. 5257–5264, Sep. 2004.

[117] R. G. Bacabac *et al.*, “Dynamic shear stress in parallel-plate flow chambers,” *J. Biomech.*, vol. 38, no. 1, pp. 159–167, Jan. 2005.

[118] D. P. Gaver and S. M. Kute, “A Theoretical Model Study of the Influence of Fluid Stresses on a Cell Adhering to a Microchannel Wall,” *Biophys. J.*, vol. 75, no. 2, pp. 721–733, Aug. 1998.

[119] E. Décavé, D. Garrivier, Y. Bréchet, F. Bruckert, and B. Fourcade, “Peeling Process in Living Cell Movement Under Shear Flow,” *Phys. Rev. Lett.*, vol. 89, no. 10, p. 108101, Aug. 2002.

[120] D. Garrivier, E. Décavé, Y. Bréchet, F. Bruckert, and B. Fourcade, “Peeling model for cell detachment,” *Eur. Phys. J. E*, vol. 8, no. 1, pp. 79–97, May 2002.

[121] J. Wong, A. Chilkoti, and V. T. Moy, “Direct force measurements of the streptavidin–biotin interaction,” *Biomol. Eng.*, vol. 16, no. 1, pp. 45–55, Dec. 1999.

[122] A. Chilkoti, T. Boland, B. D. Ratner, and P. S. Stayton, “The relationship between ligand-binding thermodynamics and protein-ligand interaction forces measured by atomic force microscopy,” *Biophys. J.*, vol. 69, no. 5, pp. 2125–2130, Nov. 1995.

[123] M. de Odrowaz Piramowicz, P. Czuba, M. Targosz, K. Burda, and M. Szymoński, “Dynamic force measurements of avidin-biotin and streptavdin-biotin interactions using AFM,” *Acta Biochim. Pol.*, vol. 53, no. 1, pp. 93–100, 2006.

[124] K. W. Oh, K. Lee, B. Ahn, and E. P. Furlani, “Design of pressure-driven microfluidic networks using electric circuit analogy,” *Lab. Chip*, vol. 12, no. 3, pp. 515–545, 2012.

[125] R. Amin *et al.*, “3D-printed microfluidic devices,” *Biofabrication*, vol. 8, no. 2, p. 022001, 2016.

[126] X. Chen and T. Li, “A novel design for passive misscromixers based on topology optimization method,” *Biomed. Microdevices*, vol. 18, no. 4, p. 57, Aug. 2016.

[127] G. Cai, L. Xue, H. Zhang, and J. Lin, “A Review on Micromixers,” *Micromachines*, vol. 8, no. 9, p. 274, Sep. 2017.

[128] M. M. Gong and D. Sinton, “Turning the Page: Advancing Paper-Based Microfluidics for Broad Diagnostic Application,” *Chem. Rev.*, vol. 117, no. 12, pp. 8447–8480, Jun. 2017.

[129] A. K. Au, W. Lee, and A. Folch, “Mail-order microfluidics: evaluation of stereolithography for the production of microfluidic devices,” *Lab. Chip*, vol. 14, no. 7, pp. 1294–1301, 2014.

[130] N. P. Macdonald, J. M. Cabot, P. Smejkal, R. M. Guijt, B. Paull, and M. C. Breadmore, “Comparing Microfluidic Performance of Three-Dimensional (3D) Printing Platforms,” *Anal. Chem.*, vol. 89, no. 7, pp. 3858–3866, Apr. 2017.